

AD-A031 255

DCW INDUSTRIES SHERMAN OAKS CALIF

NUMERICAL SIMULATION OF NOSETIP TRANSITION: MODEL REFINEMENT AN--ETC(U)

JUL 76 D C WILCOX, T L CHAMBERS

F44620-74-C-0048

UNCLASSIFIED

DCW-R-03-04

AFOSR-TR-76-1112

F/G 20/4

NL

1 OF 1
AD
A031255



AD A031255

Ag. 




DCW INDUSTRIES

DDC
RECEIVED
OCT 27 1976
D


13535 VENTURA BLVD., SUITE 207, SHERMAN OAKS, CALIF. 91423

APPROVED FOR PUBLIC RELEASE; DISTRIBUTION UNLIMITED.

1473



QUALIFIED REQUESTORS MAY OBTAIN ADDITIONAL COPIES
FROM THE DEFENSE DOCUMENTATION CENTER, ALL OTHERS
SHOULD APPLY TO THE NATIONAL TECHNICAL INFORMATION
SERVICE.

CONDITIONS OF REPRODUCTION

REPRODUCTION, TRANSLATION, PUBLICATION, USE AND
DISPOSAL IN WHOLE OR IN PART BY OR FOR THE UNITED
STATES GOVERNMENT IS PERMITTED.

AIR FORCE OFFICE OF SCIENTIFIC RESEARCH (AFSC)
NOTICE OF TRANSMITTAL TO DDC
This technical report has been reviewed and is
approved for public release IAW AFR 190-12 (7b).
Distribution is unlimited.
A. D. BLOSE
Technical Information Officer

NTIS	White Section	<input checked="" type="checkbox"/>
DOC	Buff Section	<input type="checkbox"/>
UNANNOUNCED		<input type="checkbox"/>
JUSTIFICATION.....		
BY.....		
DISTRIBUTION/AVAILABILITY CODES		
SPECIAL HANDLING SPECIAL		
A		

AFOSR-TR-76-
DCW-R-03-04

AFOSR - TR - 76 - 1112

NUMERICAL SIMULATION OF NOSETIP
TRANSITION: MODEL REFINEMENT
AND VALIDATION

by

D.C. Wilcox and T.L. Chambers

FINAL SCIENTIFIC REPORT

July 1976

Prepared for

AIR FORCE OFFICE OF SCIENTIFIC RESEARCH
Air Force Systems Command
Bolling AFB, Washington, D.C.

and

SPACE AND MISSILE SYSTEMS ORGANIZATION
Air Force Systems Command
El Segundo, California

Under Contract F44620-74-C-0048

DISTRIBUTION STATEMENT A
Approved for public release;
Distribution Unlimited

DCW Industries

13535 Ventura Boulevard, Suite 207
Sherman Oaks, California 91423
(213) 990-2682

DDC
RECEIVED
OCT 27 1976
RECEIVED
D

UNCLASSIFIED

SECURITY CLASSIFICATION OF THIS PAGE (When Data Entered)

19 REPORT DOCUMENTATION PAGE		READ INSTRUCTIONS BEFORE COMPLETING FORM	
1. REPORT NUMBER AFOSR-TR-76-1112 /	2. GOVT ACCESSION NO.	3. RECIPIENT'S CATALOG NUMBER 9	
4. TITLE (and Subtitle) NUMERICAL SIMULATION OF NOSETIP TRANSITION: MODEL REFINEMENT AND VALIDATION.		5. TYPE OF REPORT & PERIOD COVERED FINAL rept. 15 Jul 1975 / 15 Jul 1976	
7. AUTHOR(s) D. C. WILCOX T. L. CHAMBERS	12 92p.	6. PERFORMING ORG. REPORT NUMBER DCW-R-03-04	
9. PERFORMING ORGANIZATION NAME AND ADDRESS DCW INDUSTRIES 13535 VENTURA BLVD, SUITE 207 SHERMAN OAKS, CALIFORNIA 91423	16 AF-9781	8. CONTRACT OR GRANT NUMBER(s) F44620-74-C-0048	
11. CONTROLLING OFFICE NAME AND ADDRESS AIR FORCE OFFICE OF SCIENTIFIC RESEARCH/NA BLDG 410 BOLLING AIR FORCE BASE, D C 20332	11	10. PROGRAM ELEMENT, PROJECT, TASK AREA & WORK UNIT NUMBERS 681307 9781-02 61102F 17 978102	
14. MONITORING AGENCY NAME & ADDRESS (if different from Controlling Office)		12. REPORT DATE Jul 1976	
		13. NUMBER OF PAGES 90	
		15. SECURITY CLASS. (of this report) UNCLASSIFIED	
16. DISTRIBUTION STATEMENT (of this Report) Approved for public release; distribution unlimited.		15a. DECLASSIFICATION/DOWNGRADING SCHEDULE	
17. DISTRIBUTION STATEMENT (of the abstract entered in Block 20, if different from Report)			
18. SUPPLEMENTARY NOTES			
19. KEY WORDS (Continue on reverse side if necessary and identify by block number) BOUNDARY LAYER TRANSITION TURBULENCE MODEL			
20. ABSTRACT (Continue on reverse side if necessary and identify by block number) A set of constitutive equations suitable for predicting boundary-layer transition has been developed. The equations are an improved version of the turbulence-model equations devised by Saffman and Wilcox. Detailed study of the viscous sublayer of a turbulent boundary layer establishes suitable viscous modifications to the high-Reynolds-number form of the equations. Analysis of the sublayer also establishes boundary conditions suitable for surfaces with roughness and mass injection. Additional modifications based on linear stability theory obviate difficulties previously encountered in treating effects on transition of pressure			

DD FORM 1 JAN 73 1473 EDITION OF 1 NOV 65 IS OBSOLETE

UNCLASSIFIED 391 224
SECURITY CLASSIFICATION OF THIS PAGE (When Data Entered)

UNCLASSIFIED

SECURITY CLASSIFICATION OF THIS PAGE(When Data Entered)

gradient and surface heat transfer. The model accurately predicts many of the salient features of incompressible boundary-layer transition including effects of freestream turbulence intensity, width of the transition region, and transitional velocity profiles. Application to the nonequilibrium relaxation of a turbulent boundary layer passing from a rough to a smooth surface demonstrates the model's ability to accurately predict surface roughness effects. Most pertinent to the overall project objectives, the model accurately simulates ground-test transition experiments on re-entry vehicle geometries, including effects of surface roughness, surface cooling, and surface mass addition.

UNCLASSIFIED

SECURITY CLASSIFICATION OF THIS PAGE(When Data Entered)

FOREWORD

This report summarizes research performed in Contract F44620-74-C-0048 during the period July 15, 1975, through July 15, 1976. The research was jointly sponsored by the Space and Missile Systems Organization (AFSC) and the Air Force Office of Scientific Research (AFSC), United States Air Force. The Air Force program monitors were Lieutenant E. Taylor of SAMSO and P. Thurston of AFOSR. Mr. W. Portenier maintained technical liaison with the Aerospace Corporation.

Study participants were D. C. Wilcox, principal investigator, T. L. Chambers and R. M. Traci. Manuscript preparation was accomplished by J. A. Jessup.

CONTENTS

SECTION		PAGE
	FOREWORD	iii
	CONTENTS	iv
	NOTATION	vi
1	INTRODUCTION	1
2	THEORETICAL CONSIDERATIONS	4
	2.1 The Turbulence/Transition Model Equations	4
	2.2 Viscous Sublayer Structure	8
	2.2.1 Equations of Motion	9
	2.2.2 Smooth-Wall Sublayer Structure....	10
	2.2.3 Viscous Modifications	11
	2.2.4 Rough-Surface Boundary Condition..	15
	2.2.5 Effects of Mass Injection	15
	2.2.6 Composite Roughness/Blowing Boundary Condition	19
	2.3 Transition Modifications	22
	2.3.1 Pressure Gradient and Heat Transfer	22
	2.3.2 Rough-Surface Boundary Conditions.	30
3	BOUNDARY LAYER APPLICATIONS	34
	3.1 The Incompressible Flat Plate Boundary Layer	34
	3.2 Compressible Boundary Layer with Heat Transfer	42
	3.3 Boundary Layer Subject to a Step Change in Roughness	42
4	BLUNT-BODY APPLICATIONS	51
	4.1 PANT Ground-Test Experiments	51
	4.2 Other Test Cases	52
	4.2.1 Combined Effects of Roughness, Cooling and Mass Addition	55

CONTENTS (continued)

SECTION		PAGE
4	BLUNT-BODY APPLICATIONS (continued)	
	4.2.2 High Mach Number Combined Effects of Roughness, Cooling and Mass Addition	58
	4.2.3 Freestream Noise and Unit Reynolds Number	61
	4.2.4 Surface Mass Addition	61
	4.2.5 Nonspherical Shape	62
	4.2.6 Roughness Effects for Small k/θ ..	64
	4.2.7 Summary	65
5	DISCUSSION	68
	APPENDIX A: BOUNDARY-LAYER-EDGE TURBULENCE INTENSITY FOR RE-ENTRY VEHICLE NOSETIPS	70
	APPENDIX B: INPUT DATA FOR BLUNT-BODY TEST CASES	74
	REFERENCES	78
	BIBLIOGRAPHY	81

NOTATION

SYMBOL	DEFINITION
B'	Blowing parameter, $\rho_w v_w / \rho_e U_e C_H$
c_f	Local skin friction
C, \tilde{C}	Constant in law of the wall without, with blowing
C_F	Total skin friction [Equation (56)]
C_H	Stanton number
D	Drag per unit area
e	Specific turbulent mixing energy [Equation (12)]
e_{\max}	Maximum value of e in boundary layer
$f(\Lambda), F\{\Lambda; T_{\max}\}$	Stability functions [Equations (47)]
h	Mass averaged specific enthalpy
H	Total enthalpy
$H(\Lambda)$	Heaviside stepfunction
k	Roughness height (peak-to-valley)
k^+	Scaled roughness height [Equation (25)]
L	Roughness spacing (peak-to-peak)
M	Mach number
N_e, N_w	Roughness functions [Equations (49,50)]
p	Static pressure
p_{t_2}, p_{t_∞}	Total pressure behind shock, in freestream
Pr_L, Pr_T	Laminar, turbulent Prandtl number
q	Local heat flux [Equation (8)]
r	Radial distance from body axis
r_N	Nose radius

NOTATION (continued)

SYMBOL	DEFINITION
R_e, R_w	Parameters in model equations
Re_c	Minimum critical Reynolds number
$Re_{\hat{x}}$	Neutral stability Reynolds number
$Re_{k,x,\delta^*,\theta,\Delta x_t}$	Reynolds number based on roughness height, plate length, displacement thickness, momentum thickness, transition width
Re_T	Turbulent Reynolds number [Equation (11)]
Re_{∞}	Freestream unit Reynolds number
$Re_{\infty 1}$	Value of Re_{∞} for incipient transition
s	Arclength
S, S_B, S_R	Roughness functions [Equations (26,36,52)]
T	Mass averaged static temperature
$T_{t_{\infty}}$	Freestream total temperature
T', T'_{∞}	Turbulence intensity at boundary-layer edge, in freestream
T'_{max}	Maximum value of T' in boundary layer
u, v	Mass averaged velocity components in x,y directions
u_{τ}	Friction velocity, $\sqrt{\tau_w/\rho_w}$
U_{avg}	Average velocity [Equation (A6)]
\tilde{v}'	Mass averaged fluctuating velocity
w	Turbulent dissipation rate [Equation (13)]
x, y	Coordinate lying along, normal to a solid body
z	Axial coordinate

NOTATION (continued)

SYMBOL	DEFINITION
α, α^*	Parameters in model equations
$\alpha_\infty, \alpha_\infty^*$	Values of α, α^* for fully turbulent flows
$\tilde{\alpha}$	Wave number
β, β^*	Parameters in model equations
γ	Specific heat ratio
δ	Boundary layer thickness
δ^*	Displacement thickness
ϵ	Kinematic eddy viscosity
θ	Momentum thickness
$\kappa, \tilde{\kappa}$	Karman "constant" without, with blowing
λ	Parameter in model equations
Λ	Stability parameter [Equations (47)]
μ	Molecular viscosity
ν	Kinematic molecular viscosity
Ξ	Coefficient defined in Equation (35)
$\rho, \tilde{\rho}$	Mean, instantaneous mass density
σ, σ^*	Parameters in model equations
τ	Shear stress [Equation (7)]
ϕ	Angle from centerline for spheres; local body angle for laminar stable shape configuration
ψ	Modified temperature ratio [Equation (66)]
ω	Pseudovorticity
Ω	Specific pseudovorticity
ℓ	Turbulent length scale [Equation (9)]

NOTATION (concluded)

SUBSCRIPTS

DEFINITION

e	Boundary-layer edge
t	Transition point
w	Body surface
∞	Freestream

1. INTRODUCTION

During the past two-and-a-half years the authors have sought in this project to develop an accurate and efficient tool for predicting boundary-layer transition on re-entry vehicle nose-tips. The basis of our approach has been a phenomenological turbulence model developed by Saffman¹ and Wilcox.² Unlike linear stability theory, the turbulence model approach includes a description of the nonlinear growth of transition triggering disturbances; the turbulence model approach thus provides a description of boundary-layer evolution from the laminar state, through transition, and into the turbulence regime. In order for such a comprehensive theory to remain tractable, considerable engineering judgment and approximation has been needed. Including nonlinear effects, for example, is achieved through the introduction of several empirical closure coefficients. The notion that the same values of these coefficients should be used for all flows has been a central axiom in our philosophy of developing the turbulence-model transition-prediction method.

The goals of our transition research have actually been part of a much broader objective. Specifically, our primary aim has been to devise a set of constitutive equations suitable for predicting salient features of practical engineering flowfields which are dominated by turbulence and transition phenomena and which include complicating effects such as surface roughness, surface mass and heat transfer, boundary-layer separation, streamline curvature, etc. Various agencies have supported our research efforts (most notably the NASA Ames Research Center), and as a result we have made significant advances toward achieving our basic objective.

The reports and papers listed in the Bibliography provide evidence of our progress in treating the transition problem.

Using the Saffman-Wilcox turbulence model with relatively straightforward modifications to account for low-Reynolds-number effects, we have accurately predicted transition for conventional boundary layers and for ground tests on re-entry vehicle geometries. Our predictions have included most of the effects pertinent to re-entry vehicles including surface roughness, surface cooling, pressure gradient, freestream turbulence intensity, and freestream unit Reynolds number. While these results are encouraging, the number of closure coefficients has increased. Furthermore, values for some of the coefficients have been fixed by numerical experimentation, i.e., by forcing agreement of theoretical predictions with experimental data. Additionally, purely empirical modifications to the model are required to accurately predict effects of pressure gradient and surface heat transfer on boundary-layer transition. Thus, even with the model's recorded success in predicting transition, there is room for further improvement of the theory.

An important development³ in our NASA Ames-sponsored turbulence research (Contract NAS2-8884) produced significant improvement in our turbulence model's accuracy for turbulent boundary layers. Most significantly, the model's sensitivity to initial and boundary conditions, a sensitivity which has caused difficulty in our transition research,^{4,5} has been reduced markedly. Encouraged by this success, the present study has focused upon the revised model equations' accuracy for transitional flows. As will be shown in the following sections, the revised model is superior to the original model in several important respects. First, with no transition-specific modifications, the model accurately predicts many important features of an incompressible flat-plate boundary layer (FPBL) undergoing transition, viz, velocity profiles, skin friction, and transition width. Second, with modifications tied closely to

linear-stability theory, the model accurately predicts effects of pressure gradient and surface heat transfer. Third, effects of surface mass addition have been incorporated in the theory. Perhaps most important however, while the number of closure coefficients remains approximately the same as in the Saffman-Wilcox model, virtually all of the coefficients' values have been determined by methods more rigorous than numerical experimentation.

Section 2 summarizes the model equations and presents a detailed study of viscous sublayer structure; unlike the original model, analysis of the viscous sublayer provides a suitable method for treating low Reynolds number effects. The section also discusses (a) boundary conditions for surfaces with roughness and mass transfer and (b) modifications needed to accurately predict effects of pressure gradient and surface mass addition. Section 3 presents boundary-layer applications including the incompressible FPBL, effects of surface cooling on a supersonic boundary layer, and nonequilibrium relaxation of a turbulent boundary layer passing from a rough to a smooth surface. In Section 4, applications to blunt body flows are presented including effects on transition of surface roughness, cooling, and mass addition; freestream turbulence intensity; and freestream unit Reynolds number. The concluding section summarizes results and conclusions.

2. THEORETICAL CONSIDERATIONS

The model equations are summarized in this section including established values of all closure coefficients. Subsection 2.1 presents physical meanings of turbulence field properties and a discussion of similarities and differences between the new model and its predecessor, the Saffman-Wilcox^{1,2,4-6} model. Subsection 2.2 gives details of model-predicted viscous sub-layer structure, including boundary conditions for surfaces with roughness and mass addition. The section concludes with discussion of special modifications needed to obtain accurate predictions for effects on transition of pressure gradient, surface heat transfer, and surface roughness.

2.1 THE TURBULENCE/TRANSITION MODEL EQUATIONS

Under the standard boundary-layer approximations, the model equations for two-dimensional ($j=0$) and axisymmetric ($j=1$) flows are

Mass Conservation

$$\frac{\partial}{\partial x}(\rho u) + \frac{1}{r^j} \frac{\partial}{\partial y}(r^j \rho v) = 0 \quad (1)$$

Momentum Conservation

$$\rho u \frac{\partial u}{\partial x} + \rho v \frac{\partial u}{\partial y} = - \frac{dp}{dx} + \frac{\partial \tau}{\partial y} \quad (2)$$

Energy Conservation

$$\rho u \frac{\partial h}{\partial x} + \rho v \frac{\partial h}{\partial y} = u \frac{dp}{dx} + \tau \frac{\partial u}{\partial y} - \frac{\partial q}{\partial y} \quad (3)$$

Turbulent Mixing Energy

$$\rho u \frac{\partial e}{\partial x} + \rho v \frac{\partial e}{\partial y} = \left[\alpha^* \rho \left| \frac{\partial u}{\partial y} \right| - \beta^* w \right] e + \frac{\partial}{\partial y} \left[(\mu + \sigma^* \rho \epsilon) \frac{\partial e}{\partial y} \right] \quad (4)$$

Turbulent Dissipation Rate

$$\rho u \frac{\partial w^2}{\partial x} + \rho v \frac{\partial w^2}{\partial y} = \left\{ \alpha \rho \left| \frac{\partial u}{\partial y} \right| - \left[\beta + 2\sigma \left(\frac{\partial \ell}{\partial y} \right)^2 \right] w \right\} w^2 + \frac{\partial}{\partial y} \left[(\mu + \sigma \rho \epsilon) \frac{\partial w^2}{\partial y} \right] \quad (5)$$

where x and y are orthogonal coordinates with x lying along the body and y being normal to the surface; r is the radial distance from the body axis. Mass-averaged⁷ velocity components in the x and y directions are denoted by u and v while h is the mass averaged enthalpy; p , ρ and μ are mean density, pressure, and molecular viscosity; τ and q are the shear stress and normal heat flux. The mass-averaged turbulent mixing energy, e , and the mass-averaged turbulent dissipation rate, w , are needed to define the eddy diffusivity, ϵ , which is given by the following equation:

$$\epsilon = \rho e / w \quad (6)$$

The shear stress and heat flux are

$$\tau = (\mu + \rho \epsilon) \frac{\partial u}{\partial y} \quad (7)$$

$$q = - \left(\frac{\mu}{Pr_L} + \frac{\rho \epsilon}{Pr_T} \right) \frac{\partial h}{\partial y} \quad (8)$$

where Pr_L and Pr_T are laminar and turbulent Prandtl numbers. The quantity ℓ is the turbulent length scale defined as

$$\ell = \rho e^{1/2} / w \quad (9)$$

The turbulent Prandtl number, Pr_T , and the closure coefficients $\alpha, \alpha^*, \beta, \beta^*, \sigma, \sigma^*$ appearing in Equations (4) and (5) are

$$\left. \begin{aligned}
 \beta &= \frac{3}{20} & \beta^* &= \frac{9}{100} \\
 \sigma &= \frac{1}{2} & \sigma^* &= \frac{1}{2} \\
 \Pr_T &= \frac{8}{9} \\
 \alpha &= \frac{1}{3} [1 - (1 - \lambda) \exp(-\text{Re}_T/2)] \\
 \alpha^* &= \frac{3}{10} [1 - (1 - \lambda) \exp(-2\text{Re}_T)]
 \end{aligned} \right\} \quad (10)$$

where Re_T is the turbulent Reynolds number defined by

$$\text{Re}_T = \rho e^{1/2} \ell / \mu \quad (11)$$

Specification of the closure coefficient λ is deferred to Subsections 2.2 and 2.3.

Consistent with the arguments of Wilcox and Chambers,⁵ the turbulent mixing energy is proportional to the kinetic energy attending the fluctuation of fluid particles normal to the plane of shear. Letting \tilde{v}' denote the mass-averaged fluctuating velocity component normal to the shear plane (under the boundary-layer approximations, shear planes are parallel to the x direction), the turbulent mixing energy is given by

$$e = \frac{9}{4} \frac{\langle \tilde{\rho} \tilde{v}' \tilde{v}' \rangle}{\rho} \quad (12)$$

where $\tilde{\rho}$ is the instantaneous density.

The physical meaning of w has been discussed by Wilcox and Chambers.⁵ For incompressible boundary layers, comparison of the limiting forms of the model equations and the exact Reynolds stress equation very close to a solid boundary shows

that w/ρ is the rate at which e is dissipated into heat, mean kinetic energy, and other fluctuation modes. For incompressible flows, Wilcox and Chambers deduced that $w = (3\mu/\beta^*) \langle (\partial v'/\partial y)^2 \rangle / \langle v'v' \rangle$. In terms of present notation, a suitable definition of w for compressible flows is

$$w = \frac{3\mu}{\beta^*} \frac{\langle \tilde{\rho} (\partial \tilde{v}' / \partial y)^2 \rangle}{\langle \tilde{\rho} \tilde{v}' \tilde{v}' \rangle} \quad (13)$$

On the one hand, Equations (1-11) are very similar to the model equations developed by Saffman and Wilcox.^{1,2,4-6} The new model is, in fact, offered as the next-generation improvement over the Saffman-Wilcox model. The most notable similarity is the use of the dissipation-rate, w , which is analogous to the frequency or pseudovorticity quantity first introduced by Kolmogorov.⁸ Also, the high Reynolds number (i.e., $Re_T \rightarrow \infty$) values of the closure coefficients defined in Equations (10) have been determined by the same arguments based on general properties of turbulent flows used by Saffman¹ and subsequently by Wilcox and Alber.⁹

On the other hand, Equations (1-11) include several differences from the Saffman-Wilcox model which result in significant improvement in accuracy and utility. The most important difference is appearance of the term proportional to $(\partial \ell / \partial y)^2$ in Equation (5). This term has an important impact on model-predicted defect-layer structure for an incompressible FPBL. Physical meaning and origin of the term have been discussed in detail by Wilcox and Chambers.³ A second key difference is in the dimensions of the dissipation-rate quantity, w . Its dimensions are (M/L^3t) which contrasts with the specific pseudovorticity, $\Omega(L^3/Mt)$, used by Wilcox and Alber⁹ and the pseudovorticity, $\omega(1/t)$, of Saffman.¹ As shown by Wilcox and Traci,¹⁰ achieving accuracy suitable for general engineering applications involving compressible flow is contingent upon

using $w \sim \rho \omega$ rather than ω or $\Omega \sim \omega/\rho$. The final noteworthy difference is in the variation of α and α^* with Re_T . As shown in Equations (10), α and α^* approach their high Reynolds number values for $Re_T = O(1)$. This is physically more plausible than α and α^* achieving their $Re_T \rightarrow \infty$ values when $Re_T = O(10^{-1})$ as they do in the Saffman-Wilcox model.^{4,5}

In developing the new model, Wilcox and Chambers³ concentrated upon the high-Reynolds-number ($Re_T \rightarrow \infty$) form of Equations (1-11). Values of all the closure coefficients in the limit $Re_T \rightarrow \infty$ have been established by arguments based on general properties of turbulent flows. The viscous modifications, i.e., the postulated variation of α and α^* with Re_T was devised in the present study by analyzing the viscous sublayer. The next subsection presents details of model-predicted sublayer structure and rationale for the viscous modifications.

2.2 VISCOUS SUBLAYER STRUCTURE

To analyze the viscous sublayer, solutions are first presented for a perfectly smooth wall; the constant in the law of the wall, C , is found to be significantly larger than measured smooth-wall values when α^* and α assume their high-Reynolds-number values. Viscous modifications for α and α^* are then devised which yield a more-reasonable smooth-wall value for C ; detailed comparisons are made between computed and measured sublayer structure. Next, a surface dissipation-rate boundary condition is developed which is suitable for turbulent boundary layers on rough surfaces. Effects of mass injection on sublayer structure are then analyzed; a surface dissipation-rate boundary condition is devised to account for such effects on turbulent boundary layers. We conclude the section by postulating a composite roughness/mass-injection surface boundary condition for the dissipation rate.

2.2.1 Equations of Motion

In the viscous sublayer of an incompressible turbulent boundary layer, convective terms are negligible so that the equations of motion become

$$(v + \epsilon) \frac{du}{dy} = u_\tau^2 \quad (14)$$

$$\left\{ \alpha^* \left| \frac{du}{dy} \right| - \beta^* \frac{w}{\rho} \right\} e + \frac{d}{dy} \left[(v + \sigma^* \epsilon) \frac{de}{dy} \right] = 0 \quad (15)$$

$$\left\{ \alpha \left| \frac{du}{dy} \right| - \left[\beta + 2\sigma \left(\frac{d\ell}{dy} \right)^2 \right] \frac{w}{\rho} \right\} w^2 + \frac{d}{dy} \left[(v + \sigma \epsilon) \frac{dw^2}{dy} \right] = 0 \quad (16)$$

where v is kinematic viscosity and $u_\tau = \sqrt{\tau_w/\rho}$ is friction velocity. Five boundary conditions must be specified for this fifth-order set of ordinary differential equations. Two boundary conditions follow from asymptotic behavior of solutions to the model equations as $u_\tau y/v \rightarrow \infty$. Noting that turbulent-energy diffusion is negligible in this limit, there follows

$$e \rightarrow u_\tau^2/\alpha_\infty^*, \quad w \rightarrow \rho u_\tau/\alpha_\infty^* \kappa y \quad \text{as} \quad u_\tau y/v \rightarrow \infty \quad (17)$$

where $\alpha_\infty^* = 3/10$ is the limiting value of α^* for $Re_T \rightarrow \infty$. Note that Equations (17) are consistent with the law of the wall, i.e.,

$$\frac{u}{u_\tau} = \frac{1}{\kappa} \log \frac{u_\tau y}{v} + C \quad (18)$$

where $\kappa = 0.41$ is Karman's constant.

Two surface boundary conditions follow from the no-slip boundary condition which implies that u and e vanish at $y=0$. Following Saffman¹ and Saffman and Wilcox,² we impose a surface boundary condition on the dissipation rate so that

$$u = e = 0, \quad w = \frac{\rho u_\tau^2}{v \alpha_\infty^*} S_R \left(\frac{u_\tau k}{v} \right) \quad \text{at} \quad u_\tau y/v = 0 \quad (19)$$

where S_R is a universal function of the roughness height of the wall, k . As shown by Saffman and Wilcox, the constant in the law of the wall, C , depends upon S_R . Since experimental observations show that C also depends upon $u_\tau k/\nu$, comparison of computed and measured values of C establishes the dependence of S_R upon $u_\tau k/\nu$.

2.2.2 Smooth-Wall Sublayer Structure

To examine model-predicted sublayer structure, we first consider the case of a perfectly smooth wall, i.e., $S_R \rightarrow \infty$. One of the most significant results obtained by Wilcox and Saffman is that, with no viscous modifications to their model other than including molecular diffusion, the constant $C \rightarrow 5.5$ for a perfectly smooth wall. By comparison, measurements indicate that C should lie somewhere between 5 and 6. Note that Saffman and Wilcox deduced $C \rightarrow 5.7$ for perfectly smooth walls. However, in this study, Saffman-Wilcox-model computations were done using more accurate methods than those employed by Saffman and Wilcox. Our computations indicate $C \rightarrow 5.5$ in the limit of a perfectly smooth wall.

For a given value of S_R the corresponding value of C is determined by first solving the two-point boundary-value problem defined by Equations (14-17, 19), and by then evaluating the following limit:

$$C = \lim_{y^+ \rightarrow \infty} \left[\frac{u}{u_\tau} - \frac{1}{\kappa} \log \frac{u_\tau y}{\nu} \right] \quad (20)$$

where $y^+ = u_\tau y/\nu$.

The boundary value problem was solved in the present study with an implicit, second-order-accurate, time-marching, finite difference method. Initially, computations were performed with $\alpha^* = \alpha_\infty^*$ and $\alpha = \alpha_\infty$. Extrapolation of the numerical results

for large-but-finite S_R indicated that, with the new model, the limiting value of C for a perfectly smooth wall is approximately 7.0. Such a large limiting value of C is unacceptable for general engineering applications, thus prompting development of further viscous modifications to the model equations.

2.2.3 Viscous Modifications

Suitable viscous modifications are developed by noting that, as argued by Wilcox and Chambers,⁵ when $Re_T \sim 1$ net production of turbulent energy is reduced relative to the $Re_T \gg 1$ situation. This leads Wilcox and Chambers,⁵ in a prior study of boundary-layer transition, to propose a viscous modification to the Saffman-Wilcox model which reduces the production of turbulent mixing energy for small Re_T . As a generalization of Wilcox's and Chambers' viscous modification, we propose that α and α^* depend upon Re_T as follows:

$$\left. \begin{aligned} \alpha^* &= \alpha_\infty^* [1 - (1 - \lambda) \exp(-Re_T/R_e)] \\ \alpha &= \alpha_\infty [1 - (1 - \lambda) \exp(-Re_T/R_w)] \end{aligned} \right\} \quad (21)$$

Equations (21) contain three closure coefficients, i.e., λ , R_e , and R_w . The value of λ can be determined by demanding that the model equations predict that in a Blasius boundary layer turbulent fluctuations are damped for Reynolds numbers below the linear-stability-theory minimum-critical Reynolds number, Re_c . Having mixing-energy production, $\alpha^* |\partial u / \partial y|_e$, less than mixing energy dissipation, $\beta^* w_e / \rho$, insures such damping. Using the Blasius velocity profile and the smooth wall w profile (i.e., $w = 20\mu / \beta y^2$ - see Wilcox⁴ and Wilcox and Chambers⁵), the maximum plate-length Reynolds number, $Re_{\hat{x}}$, at which dissipation is greater than or equal to production throughout the boundary layer is

$$Re_{\hat{x}} \doteq 750 / \lambda^2 \quad (22)$$

The Reynolds number $Re_{\hat{x}}$ will be equal to $9 \cdot 10^4$, the accepted value of Re_c , provided

$$\lambda \doteq 1/11 \quad (23)$$

Note that in order to accurately predict effects of pressure gradient and surface heat transfer, Equation (23) must be modified. Further details are given in Subsection 2.3.

Values of R_e and R_w were chosen to achieve optimum agreement between computed and measured sublayer structure. As the first step in determining the optimum (R_e, R_w) pair, computations were performed for various values of R_e and R_w to determine pairs for which the smooth-wall value of C is within the measured range. As shown in Figure 1, a locus of values (R_e, R_w) exists which yields $C = 5.5$ for smooth walls.

The next step was to examine predicted sublayer profiles and to compare with experimental sublayer data of Laufer.¹¹ The comparisons indicated that closest agreement with Laufer's data is obtained with

$$\left. \begin{array}{l} R_e = 1/2 \\ R_w = 2 \end{array} \right\} \quad (24)$$

Figure 2 compares computed and measured velocity and shear-stress profiles and illustrates the close agreement between the computed and measured turbulent-energy production/dissipation balance.

As noted in Subsection 2.1, α and α^* approach their fully turbulent ($Re_T \gg 1$) values for $Re_T = O(1)$ while, in the Saffman-Wilcox model, $\alpha = \alpha_\infty$ and $\alpha^* = \alpha_\infty^*$ for $Re_T = 10^{-1}$. Intuitively, it seems unrealistic that a flow should begin to exhibit characteristics of fully developed turbulence before the eddy

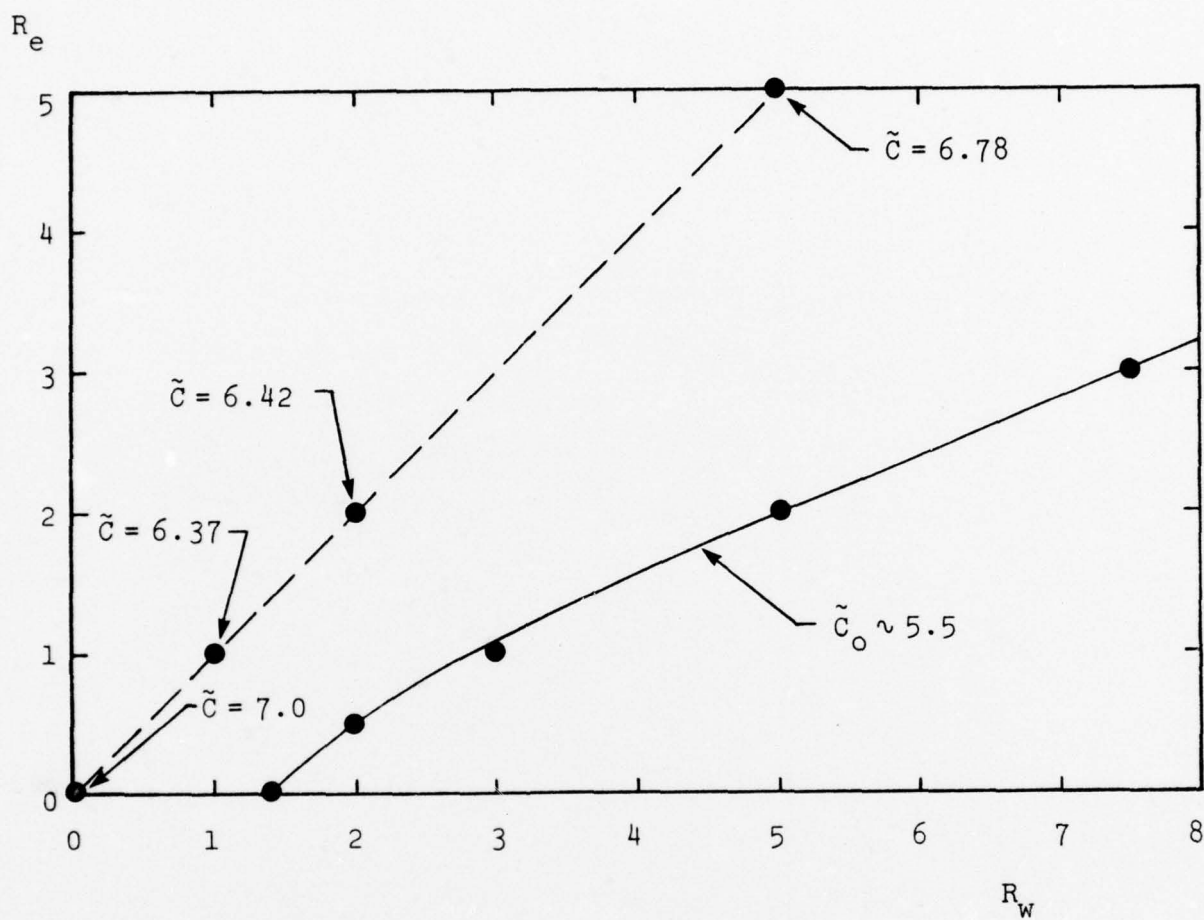


Figure 1. Variation of the smooth-wall value of C with the viscous modification constants R_e and R_w ; $R_e = R_w$ along the dashed line.

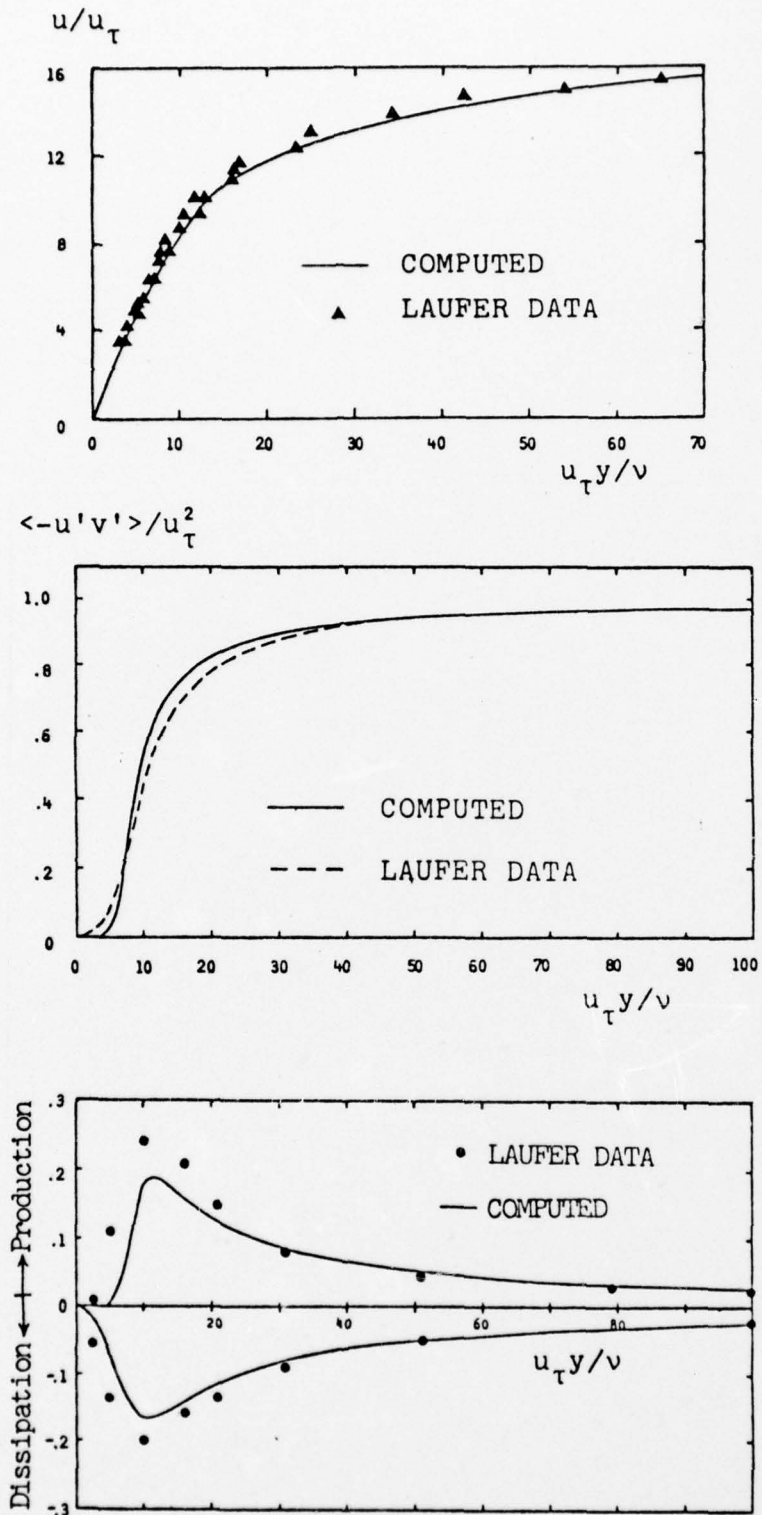


Figure 2. Comparison of computed and measured sublayer properties for a perfectly smooth wall; $R_e = 1/2$, $R_w = 2$.

diffusivity even becomes comparable to the molecular diffusivity. The viscous modifications developed here thus appear more realistic than those devised by Wilcox⁴ which, in effect, have $R_e = R_w = 1/10$. Wilcox was forced to use very small values of R_e and R_w because larger values yielded too small of a smooth-wall C . This is unsurprising in light of Figure 1. Conceivably, a similar locus of (R_e, R_w) pairs exists for the Saffman-Wilcox model, although no attempts have been made to find such pairs. The fact that the locus passes through the origin for the Saffman-Wilcox model is somewhat fortuitous.

2.2.4 Rough-Surface Boundary Condition

Having achieved acceptable smooth-wall sublayer structure, we now proceed to determine the dependence of S_R upon $u_t k/\nu$. As noted earlier in this section, C depends upon S_R which, in turn, is a function of surface roughness. Figure 3 shows the predicted variation of C with S_R ; results are similar to those obtained by Saffman and Wilcox. Sufficient experimental data¹² are available for effects of "sand-grain" roughness on turbulent boundary-layer velocity profiles to define C uniquely as a function of

$$k^+ \equiv u_t k/\nu \quad (25)$$

Comparing the measured variation of C with k^+ to the computed variation of C with S_R leads to a correlation for S_R as a function of k^+ ; Figure 3 shows the correlation. An accurate analytical fit is given by

$$S_R = (36/k^+)^2 + (8/k^+)^{1/2} \quad (26)$$

2.2.5 Effects of Mass Injection[†]

For boundary layers with surface mass injection (blowing), the introduction of an additional velocity scale (v_w = normal

[†] Results discussed in this sub-subsection were obtained under sponsorship of the NASA Langley Research Center (Contract NAS1-13974).

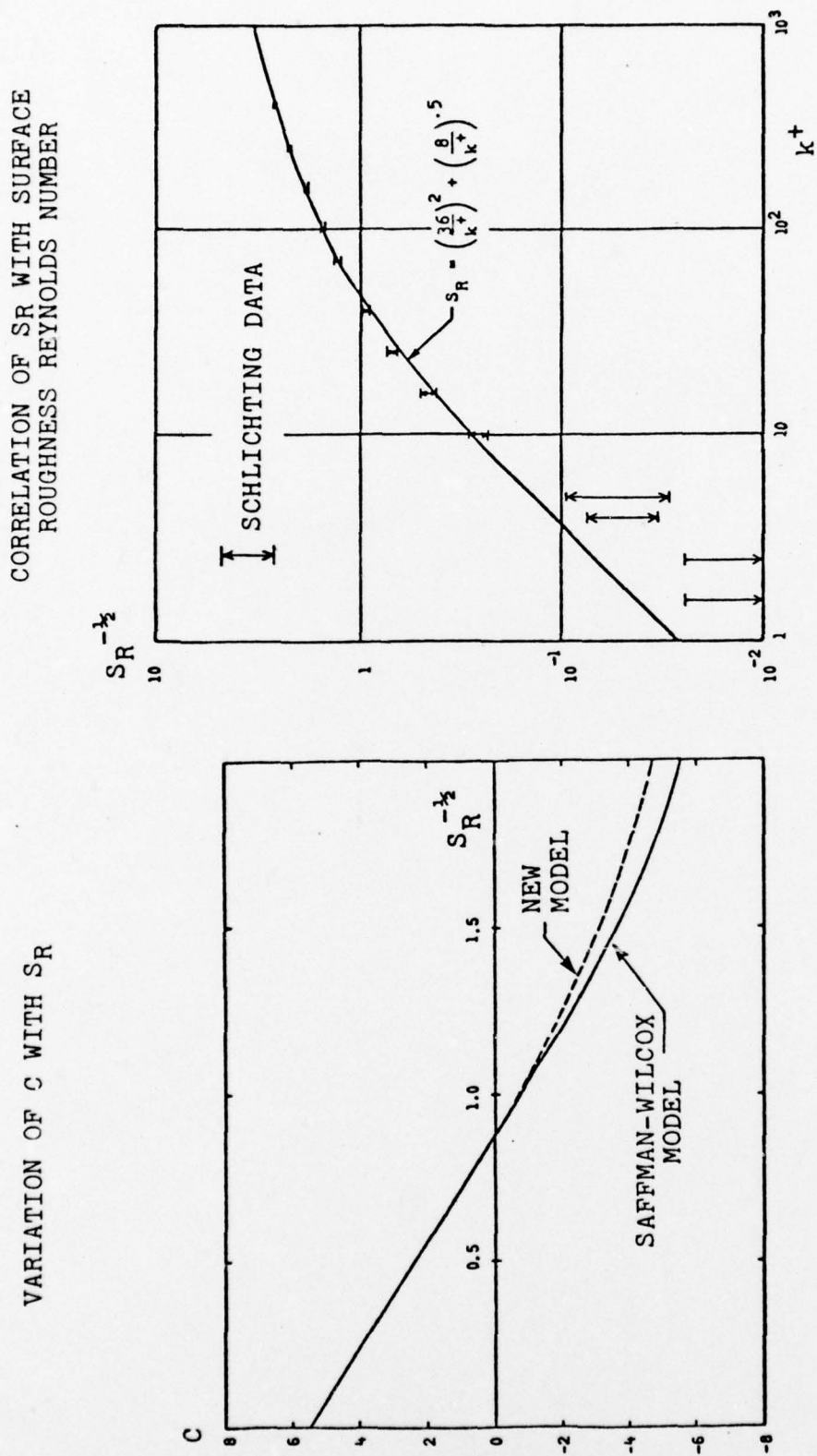


Figure 3. Basis of correlation between surface dissipation-rate boundary condition and surface roughness.

flow velocity at the surface) suggests that some modification of Equation (19) may be required for flows with blowing. Andersen, et al,¹³ provide further evidence that the dissipation-rate boundary condition must be revised when blowing is present by showing, from correlation of their experimental data, that the law of the wall assumes the following modified form:

$$\frac{u}{u_\tau} = \frac{1}{\tilde{\kappa}} \log \frac{u_\tau y}{\nu} + \tilde{C} \quad (27)$$

The modified "constants" $\tilde{\kappa}$ and \tilde{C} are related to κ , C , and the blowing velocity as follows:

$$\left. \begin{aligned} \tilde{\kappa} &= \kappa / (1 + 7.7 v_w / u_\tau) \\ \tilde{C} &= C - 50(v_w / u_\tau) + 72(v_w / u_\tau)^2 \end{aligned} \right\} \quad (28)$$

Since the computations above show that C is strongly affected by the value of S_R , Andersen's data indicate that a modification to the model equation boundary condition is required for computing blown boundary layers. Since mass injection is often pertinent for re-entry vehicles, we thus consider effects of blowing on model-predicted sublayer structure.

When blowing is present the sublayer equations are

$$(v + \epsilon) \frac{du}{dy} = u_\tau^2 + v_w u \quad (29)$$

$$v_w \frac{de}{dy} = \left\{ \alpha^* \left| \frac{du}{dy} \right| - \beta^* \frac{w}{\rho} \right\} e + \frac{d}{dy} \left[(v + \sigma^* \epsilon) \frac{de}{dy} \right] \quad (30)$$

$$v_w \frac{dw^2}{dy} = \left\{ \alpha \left| \frac{du}{dy} \right| - \left[\beta + 2\sigma \left(\frac{d\ell}{dy} \right)^2 \right] \frac{w}{\rho} \right\} w^2 + \frac{d}{dy} \left[(v + \sigma \epsilon) \frac{dw^2}{dy} \right] \quad (31)$$

To establish boundary conditions for this fifth-order system, we assume the effluent gas is free of turbulent fluctuations

so that e vanishes at the surface. The horizontal velocity, u , vanishes by virtue of the no-slip condition, and in analogy to Equation (19) we write

$$u = e = 0, \quad w = \frac{\rho u_\tau^2}{\alpha_\infty^* v} S_B \left(\frac{v_w}{u_\tau} \right) \quad \text{at} \quad u_\tau y/v = 0 \quad (32)$$

where S_B is a universal function of v_w/u_τ . Examination of asymptotic solution behavior yields two more boundary conditions valid as $u_\tau y/v \rightarrow \infty$. As in the no-blowing case, the turbulent diffusion term in the mixing-energy equation is negligible for $u_\tau y/v \rightarrow \infty$, and there follows

$$e \rightarrow \frac{u_\tau^2}{\alpha_\infty^*} \left[1 + \frac{v_w}{u_\tau} \frac{u}{u_\tau} \right], \quad w \rightarrow \frac{\rho}{\alpha_\infty^*} \frac{du}{dy} \quad \text{as} \quad u_\tau y/v \rightarrow \infty \quad (33)$$

In addition to establishing boundary conditions, further examination of the wall-layer solution (i.e., the limiting solution for $u_\tau y/v \rightarrow \infty$) demonstrates direct correspondence between model-predicted and measured effects of blowing on a turbulent boundary layer. Specifically, in the limit of weak blowing ($v_w/u_\tau \ll 1$), expanding in powers of v_w/u_τ shows that the velocity obeys a modified law of the wall similar to Equation (27). The effective Karman constant is predicted to be

$$\tilde{\kappa} = \kappa / (1 + \epsilon v_w/u_\tau) \quad (34)$$

where

$$\epsilon = \frac{4\kappa C - 1}{8\kappa} + \frac{1}{4\kappa} \log \frac{u_\tau y}{v} \quad (35)$$

The functional dependence in Equation (34) is similar to that quoted by Andersen [Equation (28)]. Table 1 shows the variation of $\tilde{\kappa}$ with $u_\tau y/v$ for $\kappa = 0.41$ and $C = 5.5$. As shown, the predicted value of $\tilde{\kappa}$ is reasonably close to Andersen's value of 7.7, particularly at the larger values of $u_\tau y/v$.

Table 1. Variation of E with $u_\tau y/\nu$.

$u_\tau y/\nu$	E
10	3.84
100	5.25
500	6.23
1000	6.65

Again using the implicit, time-marching numerical method, sub-layer calculations were performed for several blowing rates ranging from $v_w/u_\tau = 0$ to $v_w/u_\tau = 0.7393$. The value of S_B was varied for each blowing rate until close agreement with the velocity profile data of Andersen, et al,¹³ was obtained (Figure 4). As expected from the wall-layer analysis, slopes of the various profiles (i.e., $\tilde{\kappa}^{-1}$) are accurately predicted. Note that this means that, similar to the case of surface roughness, the dissipation-rate boundary condition primarily determines the variation of C with v_w/u_τ . Figure 4 also presents a correlation of S_B with v_w/u_τ ; an accurate analytical representation of the correlation is

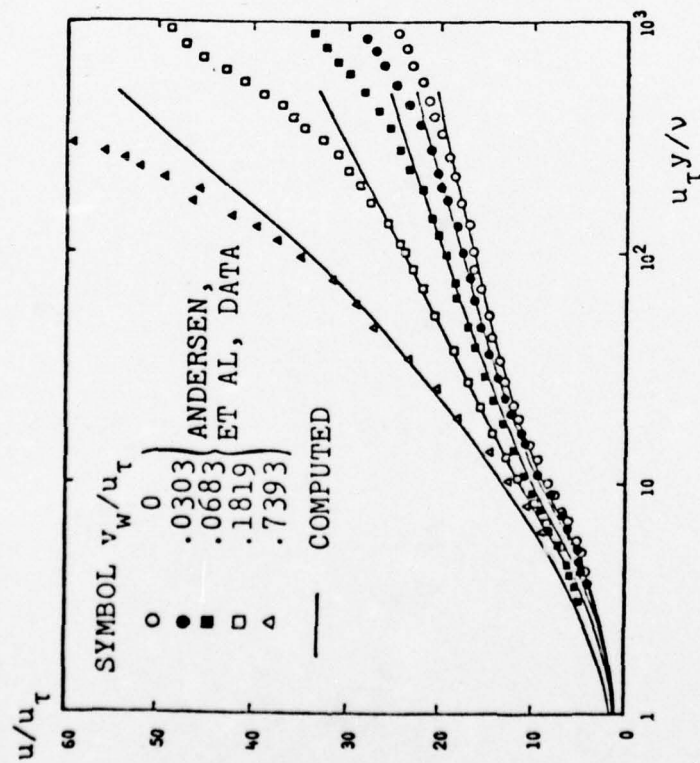
$$S_B = 6 \frac{(v_w/u_\tau)^{-1}}{1 + (v_w/u_\tau)} ; \quad v_w/u_\tau > 0 \quad (36)$$

Although effects of suction ($v_w/u_\tau < 0$) have not been considered here, computations performed by Wilcox⁴ imply that w is unaffected by suction. Therefore, Equation (36) should only be used for $v_w/u_\tau > 0$.

2.2.6 Composite Roughness/Blowing Boundary Condition

We conclude this section on model-predicted sublayer structure by postulating a dissipation-rate boundary condition suitable for surfaces with both roughness and blowing. Physical considerations must guide development of such a boundary condition.

COMPARISON OF COMPUTED AND MEASURED
SUBLAYER VELOCITY PROFILES



CORRELATION OF S_B WITH BLOWING
RATE PARAMETER, v_w/u_τ

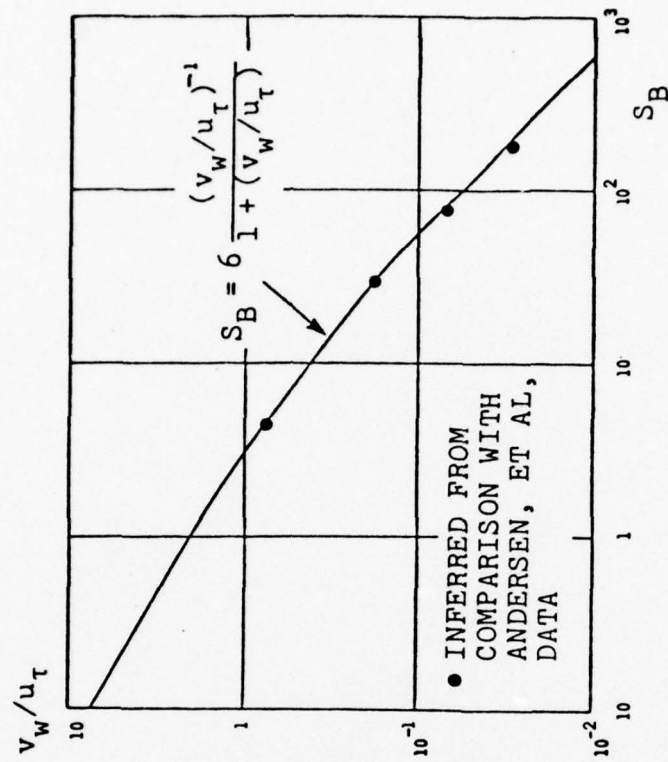


Figure 4. Basis of correlation between surface dissipation-rate boundary condition and surface mass addition rate.

For example, on extremely rough surfaces ($k^+ \rightarrow \infty$) we expect the kinetic energy of the injected fluid to be small compared to the energy attending local flow separations and turbulent fluctuations generated by the roughness elements. Effects of finite blowing rates are therefore unimportant in this limit. Similarly, for large blowing rates ($v_w/u_\tau \rightarrow \infty$), finite roughness heights have a negligible effect. Additionally, the composite boundary condition must reduce to (a) Equations (19) and (26) for $v_w/u_\tau = 0$ and (b) Equations (32) and (36) for $k^+ = 0$. The following boundary condition satisfies all of these constraints:

$$w = \frac{\rho u_\tau^2}{\alpha_\infty^* \nu} S \quad \text{at } y = 0 \quad (37)$$

where

$$S = \left(\frac{1}{S_R} + \frac{1}{S_B} \right)^{-1} \quad (38)$$

with S_R and S_B given by Equations (26) and (36).

At this point, the model has been developed with virtually no transition-specific considerations. That is, with the exception of the argument establishing the value of λ [Equation (23)], values of all closure coefficients have been fixed by arguments based on properties of fully turbulent flows. As will be shown in Section 3, the model, with no further modifications, provides an accurate description of many subtle aspects of incompressible, zero-pressure-gradient boundary-layer transition (Section 3). However, similar to the Saffman-Wilcox formulation, the new model requires modifications to the closure coefficient λ in order to accurately predict effects on transition of pressure gradient and surface heat transfer; additionally, the rough-surface boundary conditions must be revised for transition applications. Suitable modifications to λ ,

closely tied to linear stability theory, have been devised under joint sponsorship (Contract N00024-76-C-7070) of the Defense Advanced Research Projects Agency (DARPA) and the Naval Sea Systems Command (NAVSEA). Because of the pertinence of the modifications to the present study, the following subsection presents complete details before proceeding to applications in Sections 3 and 4.

2.3 TRANSITION MODIFICATIONS

In the first part of this subsection we focus on the transition modifications to the closure coefficient λ . The second part presents rough-surface boundary-condition revision needed for transition computations.

2.3.1 Pressure Gradient and Heat Transfer

As noted in the preceding section, the value of λ has been fixed by demanding that the linear-stability minimum-critical Reynolds number, Re_c , for the Blasius boundary layer match the corresponding model-equation neutral-stability Reynolds number, $Re_{\hat{x}}$. Demanding that $Re_c = Re_{\hat{x}}$ for the Blasius boundary layer yields the value of λ given in Equation (23). The model equations reasonably can be expected to apply to transitional flows which are insensitive to spectral effects. That is, the various constants in the model equations are essentially correlation coefficients which have been integrated over the turbulent spectrum. Hence, if the stability diagram shows that a wide range of wave numbers, $\tilde{\alpha}$, undergo amplification, the spectrum will more closely resemble a fully-turbulent spectrum than if only a small range of wave numbers are unstable. For example, the stability diagram for a boundary layer subjected to a pressure gradient is shown in Figure 5. For adverse pressure gradient, a finite range of wave numbers are unstable at all Reynolds numbers in excess of Re_{x_c} (note that δ^* is displacement thickness). On the basis of the discussion above, the model would be expected to accurately

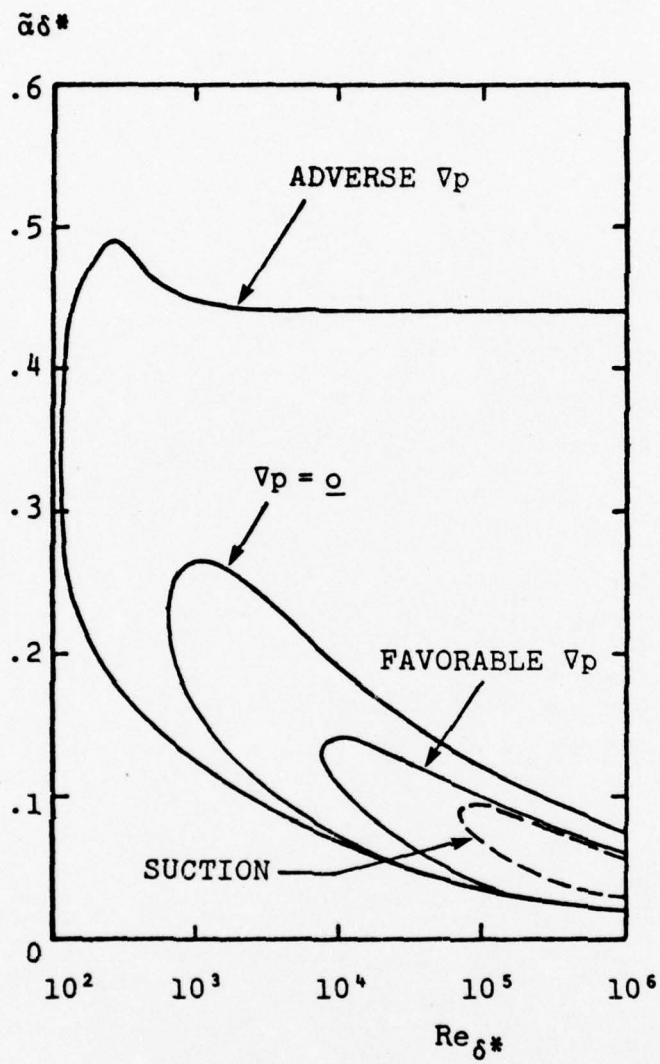


Figure 5. Neutral stability curves for laminar boundary layers with pressure gradient and suction.

predict the destabilizing effect of adverse pressure gradient. In contrast, the stability diagram becomes thinner with increasing favorable pressure gradient so that spectral effects become increasingly important, particularly for small T' which yields transition at large values of Re_{δ^*} ; the model hence would be expected to fare poorly for transitional boundary layers with favorable gradients (and low freestream disturbances).

As shown by Wilcox and Chambers,⁵ the original version of the model behaves just as the above discussion indicates. Excellent agreement between theory and experiment is obtained for adverse gradients while, for low freestream turbulence intensities, the model fails to predict the strong stabilizing effect of favorable gradient. To remove this deficiency, Wilcox and Chambers⁵ introduced an empirical modification to Equation (23). While reasonably good agreement with measurements resulted, the modification lacked rigor.

In the NAVSEA study, a better approach to modifying λ has been found. That is, the requirement

$$Re_c = Re_{\hat{x}} \quad (39)$$

has been extended to include favorable pressure gradients. Hence, for small freestream turbulence intensity we expect to have

$$\lambda = \frac{1}{11} f(\Lambda) \quad \text{as } T' \rightarrow 0 \quad (40)$$

where Λ is the modified Pohlhausen pressure gradient parameter

$$\Lambda = \frac{\rho_e \theta^2}{\rho_w v_e} \frac{dU_e}{dx} = - \frac{\rho_e \theta^2}{\rho_w U_e} \left(\frac{\partial^2 u}{\partial y^2} \right)_w \quad (41)$$

The function $f(\Lambda)$ must be determined by equating Re_c and $Re_{\hat{x}}$. Figure 6 presents results based on the Pohlhausen profiles¹⁴;

$$\Lambda = -\frac{\rho_e}{\rho_w} \frac{\theta^2}{U_e} \left(\frac{\partial^2 u}{\partial y^2} \right)_w$$

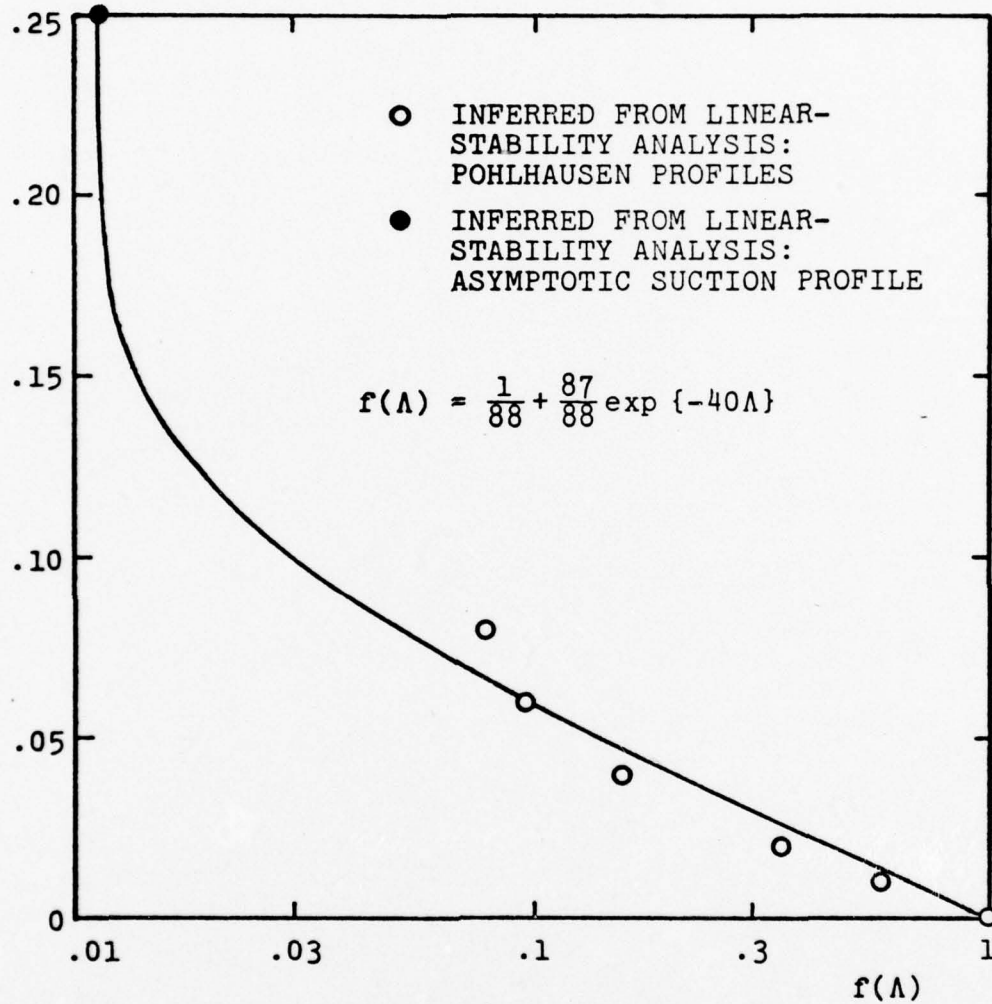


Figure 6. The stability function $f(\Lambda)$.

a good fit to the data indicate the variation of λ with Λ is hence

$$f(\Lambda) \doteq \frac{1}{88} + \frac{87}{88} \exp [-40\Lambda H(\Lambda)] \quad (42)$$

where $H(\Lambda)$ is the Heaviside stepfunction. The limiting value of $f(\Lambda)$ as $\Lambda \rightarrow 0$ has been obtained by a similar analysis of the asymptotic laminar profile for a uniformly-sucked FPBL.

Turning to heat transfer, an additional modification to λ is needed. Following Wilcox and Chambers,⁶ for incompressible aerodynamic boundary layers with heat transfer, the neutral stability Reynolds number based on wall conditions is given by

$$\text{Re}_{\hat{x}_w} \equiv \frac{U_e \hat{x}}{v_w} \doteq \frac{750}{\lambda^2} \quad (43)$$

According to linear stability theory,¹⁵ the corresponding minimum-critical Reynolds number Re_{c_w} varies as follows:

$$\text{Re}_{c_w} \sim (T_w/T_e)^{-7} \quad (44)$$

Hence, since $\mu \sim T^{0.7}$ for air, we have

$$\text{Re}_{c_w} \sim (\mu_w/\mu_e)^{-5} \quad (45)$$

We thus postulate that for flows with heat transfer, λ be written as follows:

$$\lambda = \frac{1}{11} \left(\frac{\mu_w}{\mu_e} \right)^{5/2} f(\Lambda) \quad (46)$$

Finally, note that for high freestream turbulence intensities, transition is unlikely to be sensitive to spectral effects regardless of the stability diagram. That is, typical high intensity freestream turbulence will have fluctuations at

all frequencies (wave numbers). Therefore, the modifications proposed in Equation (46) is strictly valid only at $T' \rightarrow 0$. Hence, to complete the formulation, we introduce an exponential dependence upon T'_{\max} , the maximum disturbance in the boundary layer, so that the completed formulation is as follows:

TRANSITION MODIFICATION

$$\lambda = \frac{1}{11} \left(\frac{\mu_w}{\mu_e} \right)^{5/2} F\{\Lambda ; T'_{\max}\}$$

$$F\{\Lambda ; T'_{\max}\} = 1 + [f(\Lambda) - 1] \exp[-3T'^2_{\max}]$$

$$f(\Lambda) = \frac{1}{88} + \frac{87}{88} \exp[-40\Lambda H(\Lambda)]$$

where

$$\Lambda = -\frac{\rho_e \theta^2}{\rho_w U_e} \left(\frac{\partial^2 u}{\partial y^2} \right)_w \quad \text{and} \quad T'_{\max} = 100 \sqrt{\frac{2}{3}} e_{\max} / U_e$$

(47)

Figures 7 and 8 illustrate how accurately the model predicts effects on transition of pressure gradient and heat transfer. Figure 7 compares predicted and measured effects of pressure gradient on FPBL transition. As shown in the figure, the Crabtree¹⁶ data are closely simulated by the computations with $T' = .01\%$ and $.03\%$. Since the Crabtree data are for flight tests (closed circles) and quiet wind tunnels (open circles), the value of T' for the experiments would be expected to fall in the range of $.01\%$ -. 03% . The agreement between theory and experiment hence is very good for low intensities. Additionally, the Feindt¹⁷ high-intensity data ($T' = 1.25\%$) are closely matched by the computed curve with $T' = 1.25\%$. Figure 8 compares computed and measured transition Reynolds number for low-speed aerodynamic boundary layers. The data of Zysina-Molozhen and Kuznetsova¹⁸ were taken in relatively noisy environments so that they correspond to high

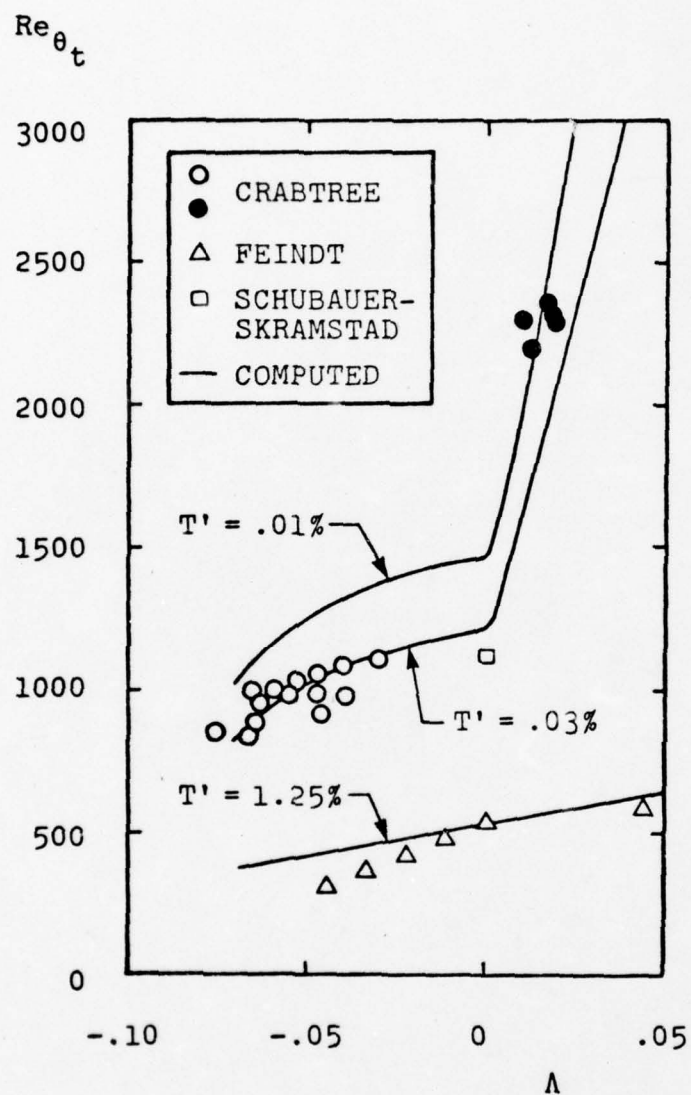


Figure 7. Comparison of computed and measured effects of pressure gradient on boundary-layer transition.

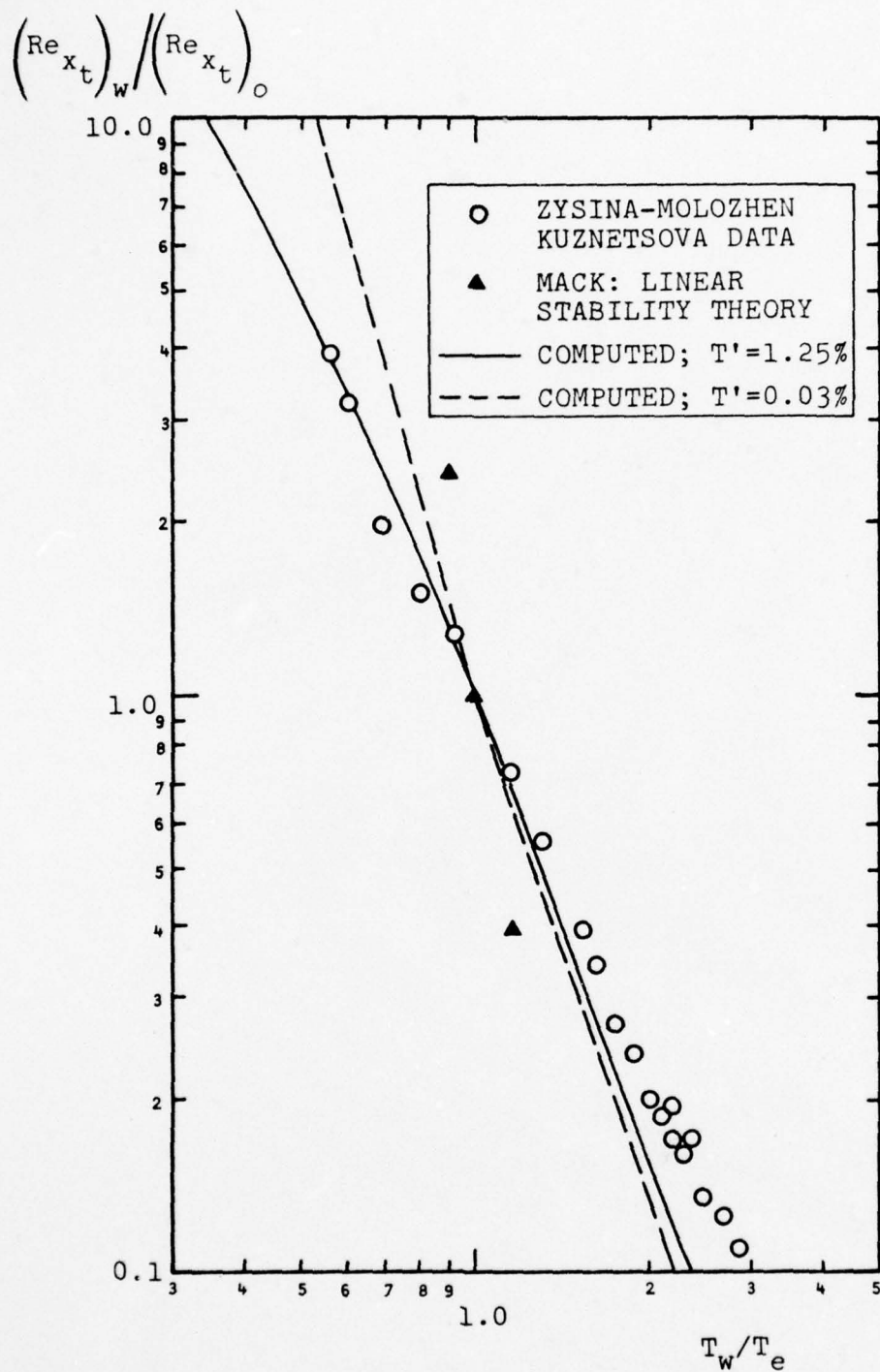


Figure 8. Comparison of computed and measured effects on transition of heat-transfer for low-speed aerodynamic boundary layers.

intensity freestream conditions. The fact that the curve computed with $T' = 1.25\%$ is close to the data is hence very encouraging. For the low intensity computations ($T' = 0.03\%$), the predicted stabilizing effect of cooling is much stronger than for the $T' = 1.25\%$ computations. As expected, the variation of $(Re_{xt})_w$ is approaching the linear stability predictions of Mack.

2.3.2 Rough-Surface Boundary Conditions

As with the Saffman-Wilcox model, the rough-surface boundary conditions for e and w must be revised for transitional flows. The primary reason for the modifications is to facilitate use of a boundary layer computation for predicting transition; use of Equations (19) would require an elliptic integration method to account for local flow separation between roughness elements. Complete discussion of this point is given by Wilcox and Chambers.⁵

Similar to the approach taken by Wilcox⁴ and by Wilcox and Chambers,⁵ we postulate that Equation (19) be replaced by

$$\left. \begin{aligned} u &= 0 \\ e &= \frac{1}{\alpha_\infty^*} \frac{v_w^2}{k^2} N_e \left(\frac{c_f}{k/\theta} \right) \\ w &= \frac{S_R}{\alpha_\infty^*} \frac{u_\tau^2}{v_w} N_w \left(\frac{c_f}{k/\theta} \right) \end{aligned} \right\} \quad (48)$$

where S_R is given by Equation (26). The functions N_e and N_w have been found by numerical experimentation; their postulated dependence upon $c_f/(k/\theta)$ is

$$N_e = \begin{cases} 0 & , \quad k^+ < 5 \\ .001 \left[\frac{275 c_f}{k/\theta} \right]^{-4} & , \quad k^+ \geq 5 \end{cases} \quad (49)$$

$$N_w = \begin{cases} 1 & , k/\theta \leq 275 c_f \\ \left[\frac{275 c_f}{k/\theta} \right]^6 & , k/\theta > 275 c_f \end{cases} \quad (50)$$

Equations (48-50) closely resemble the boundary condition revisions presented by Wilcox and Chambers.⁵ The most significant difference is in Equation (49), where e is forced to vanish for $k^+ < 5$. Having such a cutoff is equivalent to stating that below a critical Reynolds number, vortex shedding behind roughness elements ceases. The cutoff value of 5 has been established by the following argument. First, experimental measurements¹⁹ indicate that for flow past a cylinder, vortex shedding occurs only when Reynolds number based on cylinder radius exceeds about 25. Second, the corresponding Reynolds number for a roughness element is $u_k k/\nu$ where u_k is a characteristic velocity. Third, assuming the velocity varies linearly close to the wall, then $u_k \approx u_\tau^2 k/\nu$; consequently, $u_k k/\nu = (k^+)^2$ where k^+ is defined in Equation (25). Finally, requiring a cessation of vortex shedding for $u_k k/\nu < 25$ implies no vortex shedding for $k^+ < 5$.

Figure 9 shows computed effects of surface roughness on FPBL transition; experimental data of Feindt¹⁷ are shown for comparison. Freestream intensity has only a slight effect on transition Reynolds number based on plate length, Re_{x_t} , for roughness-height Reynolds numbers in excess of 300. Thus, consistent with qualitative observations, the revised model predicts existence of a roughness dominated regime, although substantiating data are unavailable for determining the minimum value of Re_k at which transition becomes roughness dominated. Also, again consistent with measurements and qualitative observations, roughness has virtually no effect on FPBL transition for $Re_k \leq 120$.

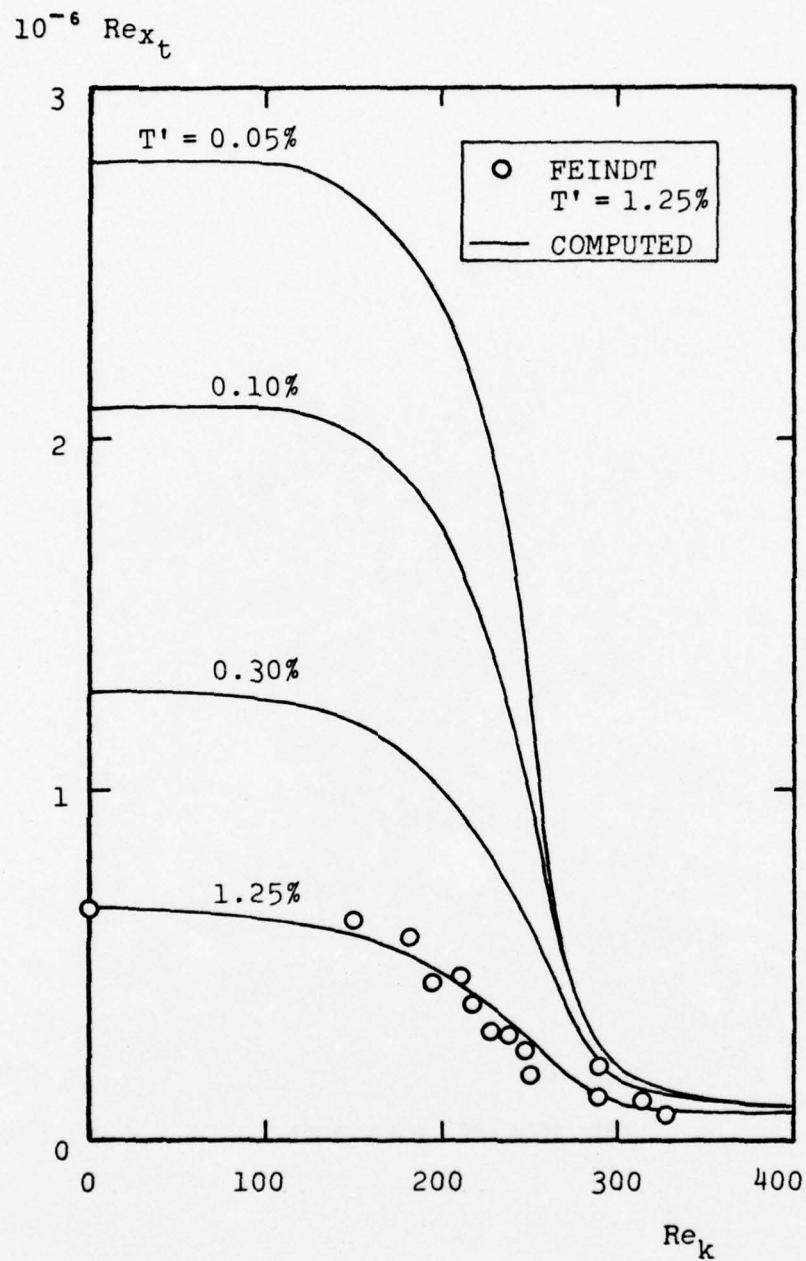


Figure 9. Effect of surface roughness on flat-plate boundary-layer transition.

The turbulence/transition model is now completely formulated. In summary (a) the completed set of model equations is given by Equations (1-11), (b) the closure coefficient λ is defined in Equation (47), and (c) surface boundary conditions for e and w are

$$\left. \begin{aligned} e &= \frac{1}{\alpha_{\infty}^*} \frac{v_w^2}{k^2} N_e \left(\frac{c_f}{k/\theta} \right) \\ w &= \frac{S}{\alpha_{\infty}^*} \frac{u_{\tau}^2}{v_w} \end{aligned} \right\} \quad (51)$$

where

$$S = \left[\frac{1}{S_B} + \frac{1}{S_R N_w} \right]^{-1} \quad (52)$$

with S_R and S_B given in Equations (26) and (36), respectively; N_e and N_w are defined by Equations (49) and (50). All of the applications in the following two sections have been done with no adjustment of the various closure coefficients.

3. BOUNDARY LAYER APPLICATIONS

To test the new model, we first consider carefully-documented experiments for conventional boundary-layers. This section presents results of three applications. First, we apply the model to an incompressible FPBL including comparisons of computed and measured transitional velocity profiles, transition width, and transition sensitivity to freestream turbulence intensity and scale. Then, we simulate the stabilizing effect of surface cooling on a supersonic boundary layer. Finally, we predict the nonequilibrium adjustment of a rough-wall turbulent boundary layer which is suddenly exposed to a smooth surface.

3.1 THE INCOMPRESSIBLE FLAT PLATE BOUNDARY LAYER

As the first step in testing the new model, we analyze various aspects of model-predicted incompressible FPBL transition. As shown in Figure 10, starting from laminar flow at the plate leading edge, the model predicts that the skin friction initially matches the Blasius value. Then, depending upon the freestream turbulence intensity, T' , defined by

$$T' = 100 \sqrt{\frac{2}{3}} e_e / U_e \quad (53)$$

the skin friction rapidly increases at a critical Reynolds number, Re_{x_t} , and asymptotically approaches the equilibrium turbulent value. Predicted variation of c_f closely resembles that observed when a boundary layer undergoes transition to turbulence.

For example, Figure 11 shows that, consistent with measurements,²⁰ momentum-thickness Reynolds number at transition, Re_{θ_t} , varies almost linearly with T' for low-intensity free-stream turbulence (i.e., T' less than 1%). (The criterion

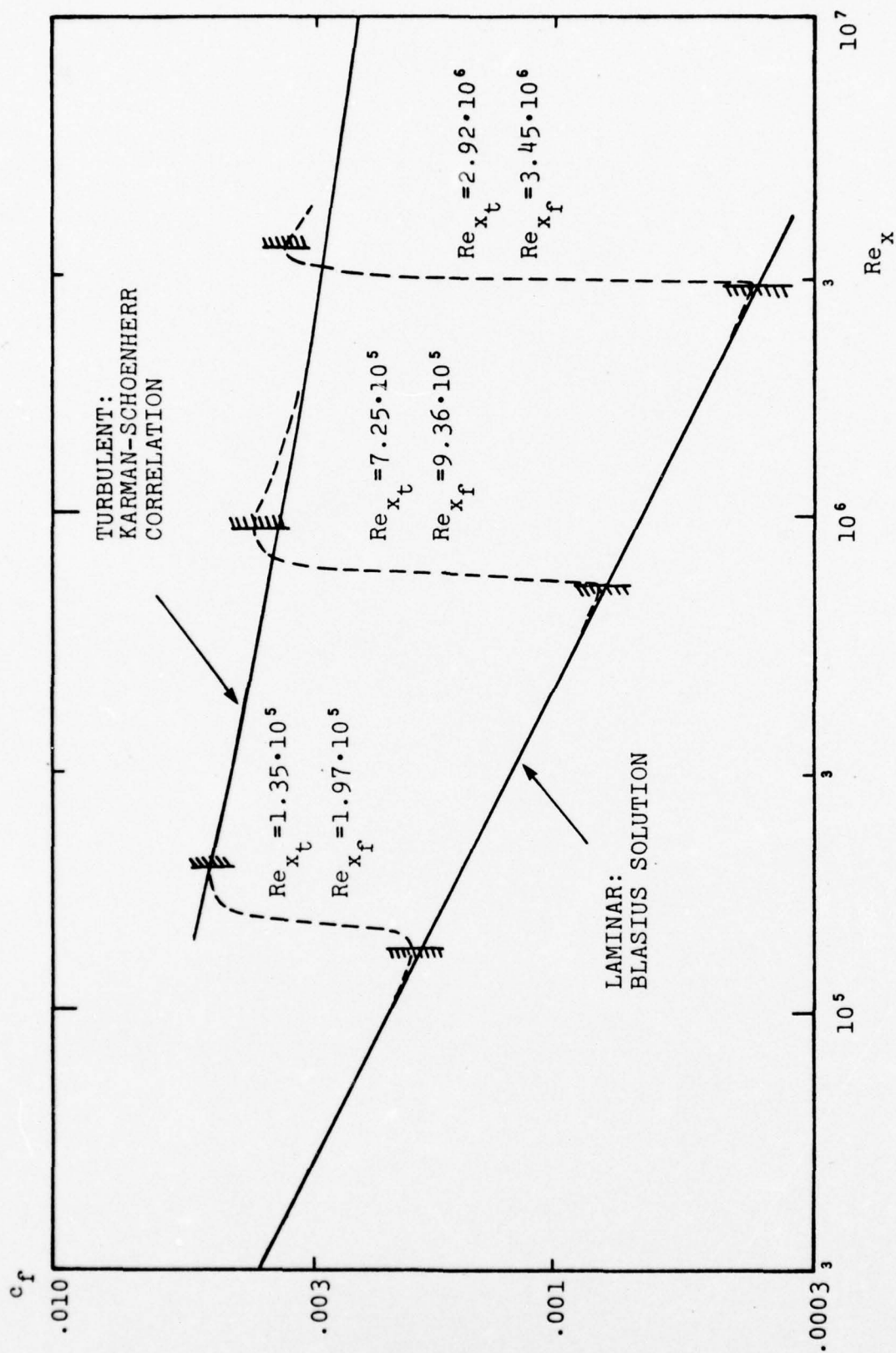


Figure 10. Computed variation of skin friction with Re_x for transitional boundary layers; transition region lies between points at which minimum and maximum c_f occur.

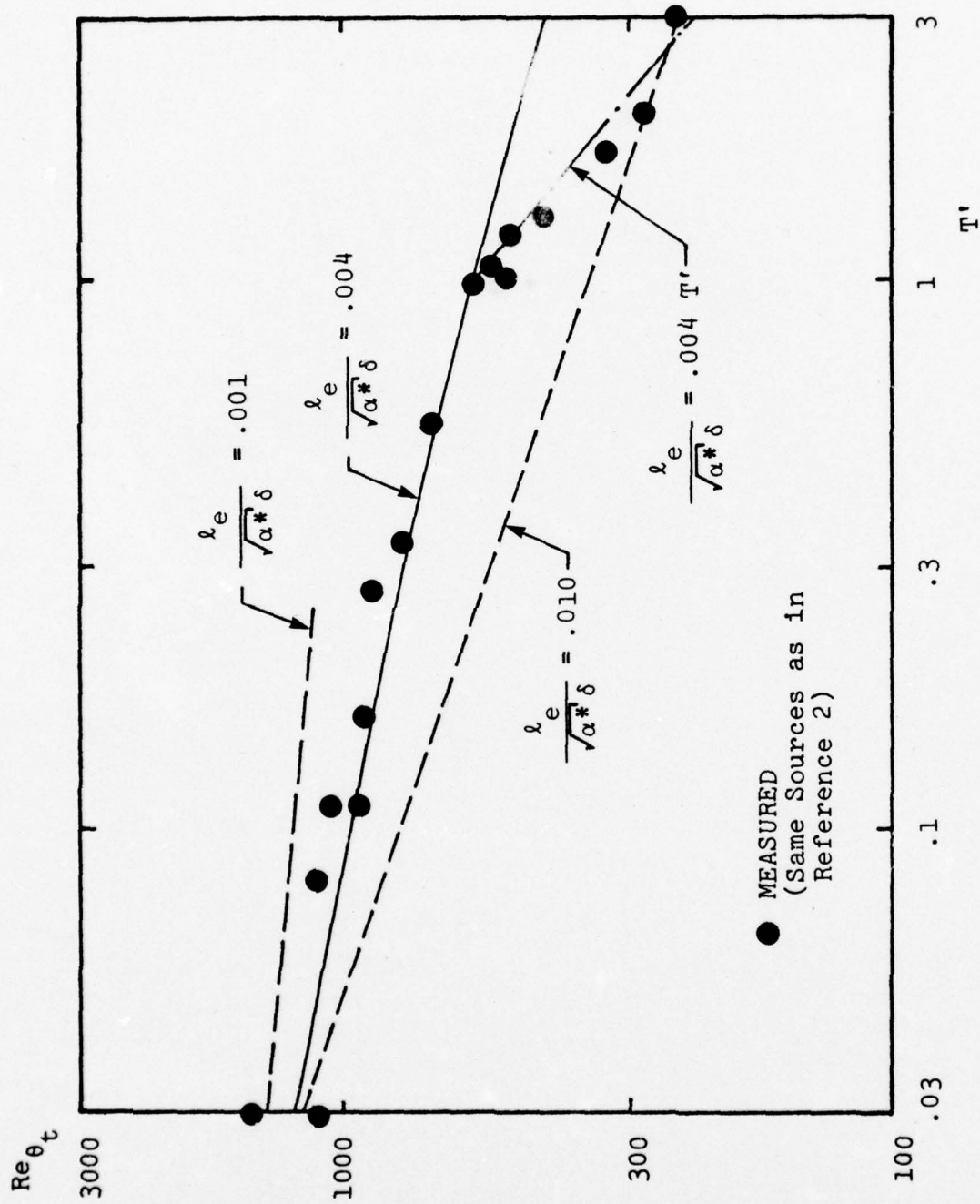


Figure 11. Effect of freestream turbulence intensity on transition location for a flat-plate boundary layer.

used to define transition is the point at which c_f achieves a minimum.) Note that turbulence scale has an effect on Re_{θ_t} , particularly for $T' > 1\%$. Computations have been performed with various ratios of $\ell_e/\sqrt{\alpha_\infty^*} \delta$ to δ ; having $\ell_e/\sqrt{\alpha_\infty^*} \delta$ given by

$$\frac{\ell_e}{\sqrt{\alpha_\infty^*} \delta} = .004 \quad ; \quad T' < 1 \quad (54)$$

most nearly matches the low-intensity values of Re_{θ_t} . Somewhat larger values of $\ell_e/\sqrt{\alpha_\infty^*} \delta$ are needed to match the high-intensity data; for values of T' in excess of 1%, excellent agreement between computed and measured Re_{θ_t} is obtained with $\ell_e/\sqrt{\alpha_\infty^*} \delta$ given by

$$\frac{\ell_e}{\sqrt{\alpha_\infty^*} \delta} = .004 T' \quad ; \quad T' > 1 \quad (55)$$

Intuitively, we expect that ℓ_e should increase with T' for high-intensity turbulence since, in the case of fully turbulent boundary layers, values of $\ell_e/\sqrt{\alpha_\infty^*} \delta$ generally are an order-of-magnitude greater than that given by Equation (54). The variation of ℓ_e with T' given by Equation (55) is quite plausible since the peak local intensity in a fully turbulent incompressible FPBL is of the order of 10 to 12% which, from Equation (55) indicates $\ell_e/\sqrt{\alpha_\infty^*} \delta$ is of the order .04 to .05. For turbulent boundary layers, $\ell_e/\sqrt{\alpha_\infty^*} \delta$ is typically .09.

In Figure 12, predicted width of the transition region is compared with measured²¹ width. Transition width, Δx_t , is defined as the distance between minimum and maximum skin-friction points. Using this definition for Δx_t , Reynolds number based on Δx_t was computed for Re_{x_t} ranging from $5.0 \cdot 10^4$ to $4.4 \cdot 10^6$. As shown, the computed curve falls within experimental data scatter.

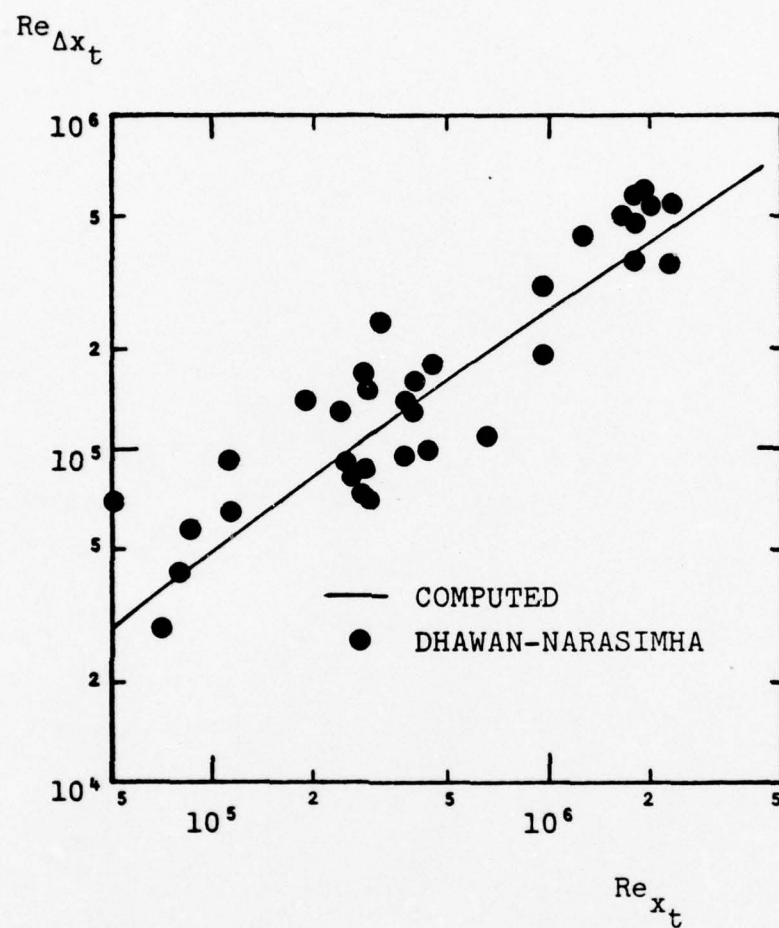


Figure 12. Comparison of computed and measured Reynolds number based on transition-zone width.

Figure 13 presents a direct comparison between computed and measured²² transitional total skin friction, C_F , defined by

$$C_F = \frac{D}{\frac{1}{2}\rho U_e^2 x} \quad (56)$$

where D is drag per unit area and x is distance from the plate's leading edge. Consistent with the data, the boundary layer is predicted to have a long memory of upstream flow conditions. That is, while transition occurs at $Re_x \doteq 4 \cdot 10^5$, the predicted C_F doesn't begin its asymptote to the fully turbulent value until $4 \cdot 10^6$, a full decade higher. The long-persisting memory of transition is also indicated in Figure 10 where the local skin-friction coefficient first overshoots and then gradually approaches the fully turbulent value. Such an overshoot in c_f is observed, particularly in supersonic boundary layers²¹; the c_f overshoot is believed to be associated with the measured higher-than-expected recovery factors near transition. Figure 14 compares the predicted and measured²¹ magnitude of the overshoot defined by

$$\frac{\Delta c_f}{c_{f_0}} \equiv \frac{c_f - c_{f_0}}{c_{f_0}} \quad (57)$$

where c_{f_0} is given by the Karman-Schoenherr²³ correlation for turbulent FPBL's. As can be seen from the figure, model predictions are close to the experimental data. A good fit to the numerical results is

$$\frac{\Delta c_f}{c_{f_0}} = .063 \log Re_{x_t} - B \quad (58)$$

where $B = 0.734$ when the transition point is defined as the point where c_f achieves a minimum and $B = 0.720$ when the transition point is defined as the point where c_f first differs from the laminar value by more than 0.5%.

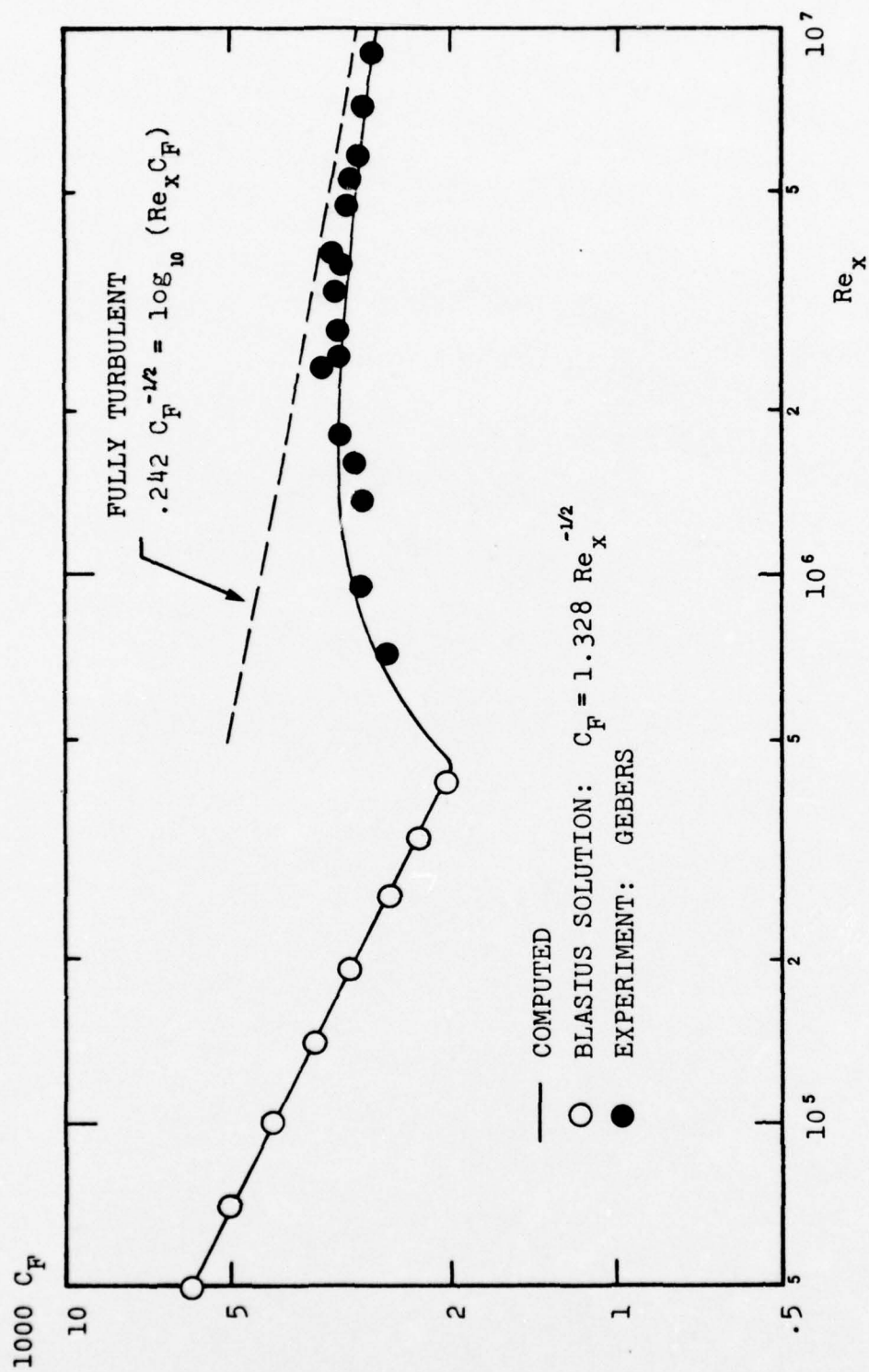


Figure 13. Comparison of computed and measured total skin friction for a transitional flat-plate boundary layer.

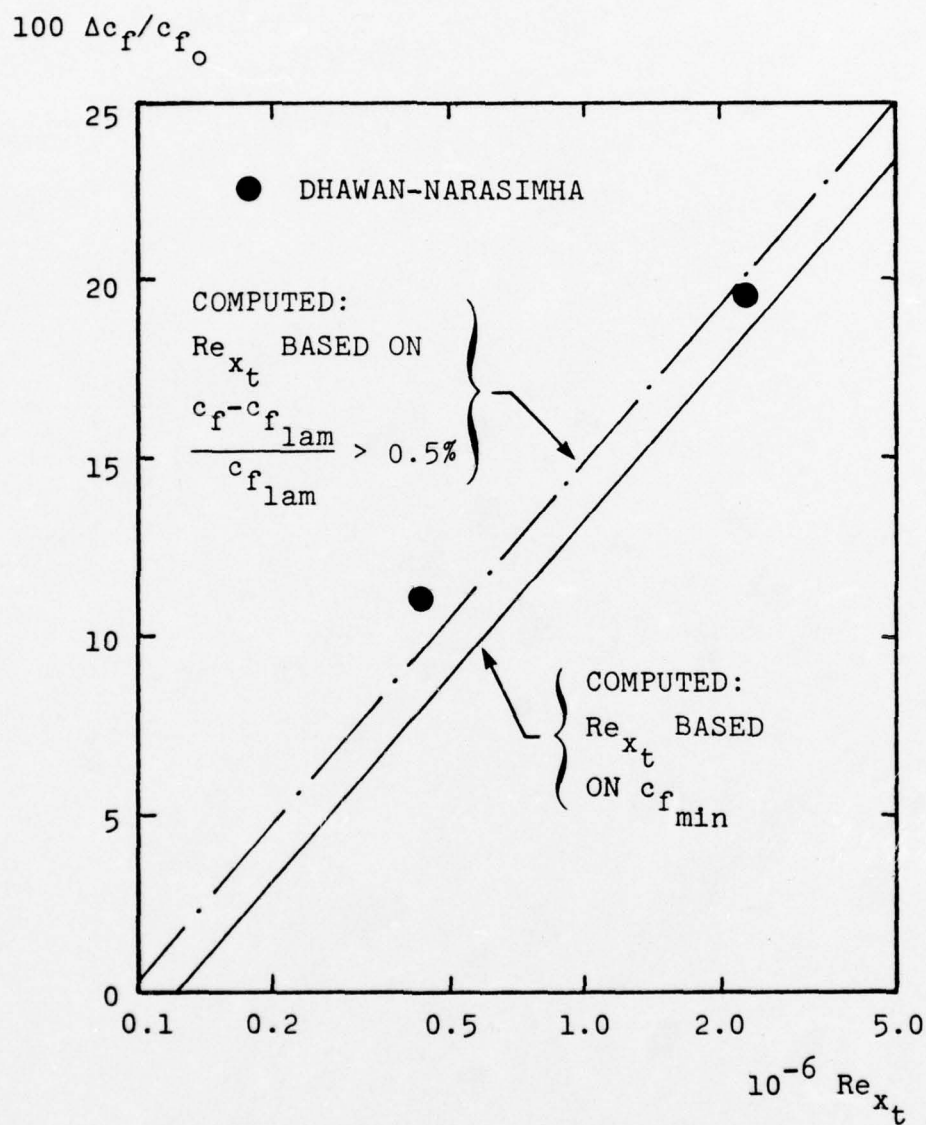


Figure 14. Comparison of computed and measured skin friction overshoot through transition for a flat-plate boundary layer.

Figure 15 exhibits computed and measured²⁴ velocity profiles through transition for $T' = .03\%$. Comparison of velocity profiles at $x = 5.75$ ft indicates the computed boundary layer goes turbulent a bit faster than measured. Proceeding downstream, however, computed and measured velocity profiles show decreasing differences until, beyond $x = 6.75$ ft, differences are less than 5%.

An interesting point about these results is that because $(\partial^2 u / \partial y^2)_w$ vanishes for incompressible FPBL flow, the transition modification defined in Equation (47) has no effect. Hence, the turbulence model as stated in Subsection 2.1 applies, with no alteration, to the incompressible FPBL.

3.2 COMPRESSIBLE BOUNDARY LAYER WITH HEAT TRANSFER

Our second application is for the effects of surface cooling on a smooth-wall, Mach 2.7 boundary layer. Figure 16 compares computed effects of cooling with the experimental data of van Driest and Boison²⁵; T_w and T_{aw} denote wall temperature and adiabatic wall temperature, respectively. Computations have been done for low ($T' = 0.01\%$) and high ($T' = 1.25\%$) freestream turbulence intensities. Consistent with measurements, cooling has a strong stabilizing effect, particularly for low freestream turbulence level. Note that, consistent with the van Driest-Boison data, the effectiveness of cooling is greatly reduced when the freestream turbulence is very intense.

3.3 BOUNDARY LAYER SUBJECT TO A STEP CHANGE IN ROUGHNESS

To test the model's ability to predict effects of surface roughness, we apply the model to the development of a turbulent rough-wall boundary layer suddenly exposed to a smooth wall. Computations simulate an experiment by Antonia and Luxton,²⁶ for which an incompressible fluid flows past a

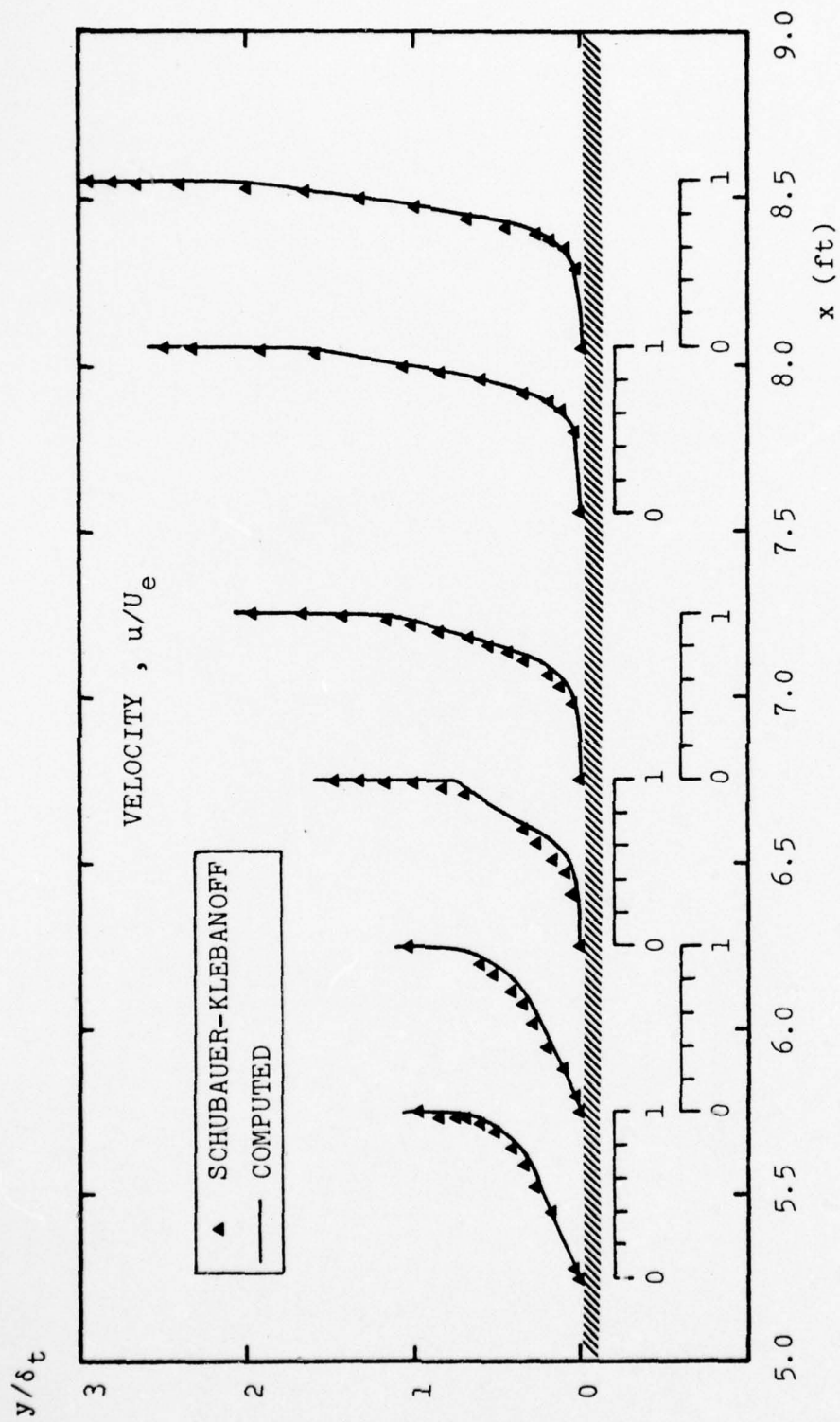


Figure 15. Comparison of computed and measured transitional velocity profiles for an incompressible flat-plate boundary layer; $T' = .03\%$; $k_e/\sqrt{\alpha_\infty} = .09$; $Re_\infty = 5.2 \cdot 10^5$ per foot.

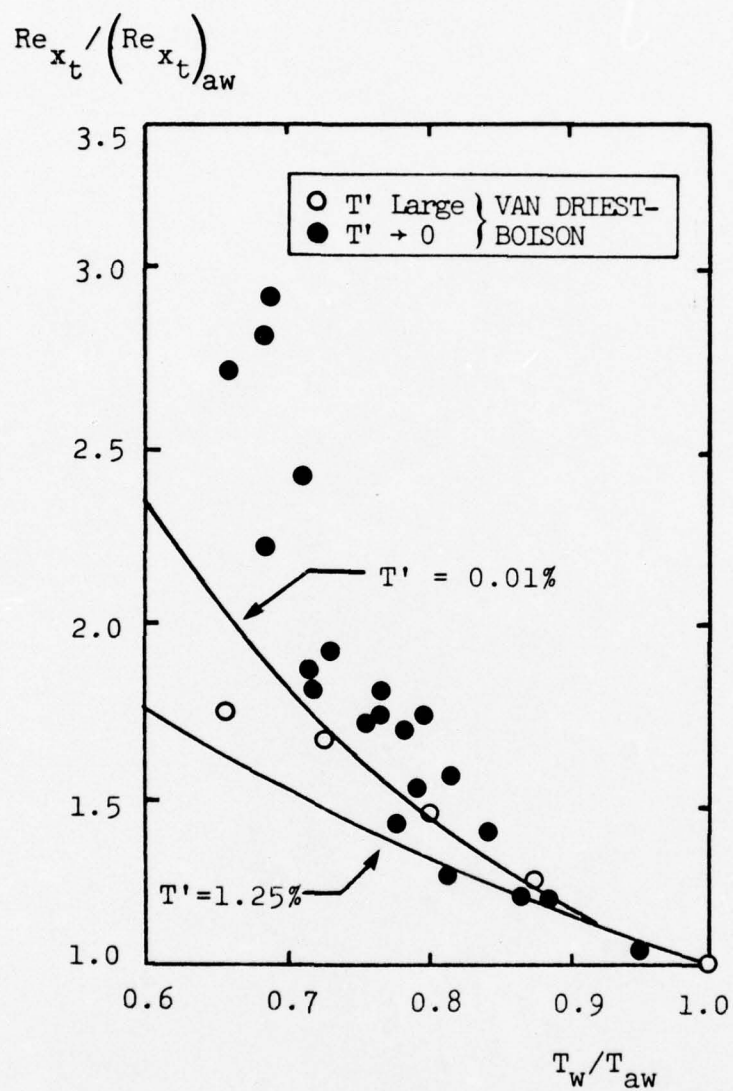


Figure 16. Comparison of computed and measured effect of surface cooling on supersonic boundary layer transition; $M_e=2.7$, $Re_\infty=8.04 \cdot 10^6/\text{ft}$.

flat plate perfectly smooth from its leading edge, $x = 0$, up to $x = 8$ ft. Between $x = 8$ ft and $x = 12$ ft, the plate is covered with distributed (square) roughness elements of height $k = 1/8$ in; peak-to-peak distance between the elements is $1/2$ in. Beyond $x = 12$ ft the plate is perfectly smooth.

The objective of the Antonia-Luxton experiment is to study boundary-layer response in the region $x > 12$ ft. The boundary layer undergoes strong departure from equilibrium as the surface changes from rough to smooth. In particular, Antonia and Luxton find that even at $x = 15.8$ ft, the farthest downstream location at which they measure, the boundary layer still has not achieved equilibrium. This flow hence presents a rigorous test of the model.

The computation was performed for the lowest of the two-unit Reynolds numbers considered by Antonia and Luxton, viz, $U_{\infty}/\nu = 1.11 \cdot 10^5 \text{ ft}^{-1}$, where U_{∞} is freestream velocity. Calculation was initiated at $x = 12$ ft from the measured u , $\langle v'^2 \rangle$, and $\langle -u'v' \rangle$ profiles. Figures 17-20 show results of the computation (note that $\delta_s = 2.8$ in. is boundary-layer thickness at $x = x_s = 12$ ft). Computed velocity profiles virtually duplicate measured profiles at all stations, except very near the wall where semilog plots indicate 10% differences. Computed and measured shape factor agree to within 3%; predicted c_f is within 20% of Preston tube measurements.

The most significant result is the predicted slow approach to equilibrium. Inspection of computed H and c_f show that, consistent with measurements, the boundary layer is still out of equilibrium 20 boundary layer thicknesses downstream of the rough-wall/smooth-wall juncture. Discrepancies between computed and measured c_f are unalarming because Antonia and Luxton indicate that the measurements are unreliable for $(x - x_s)/\delta_s \leq 2$.

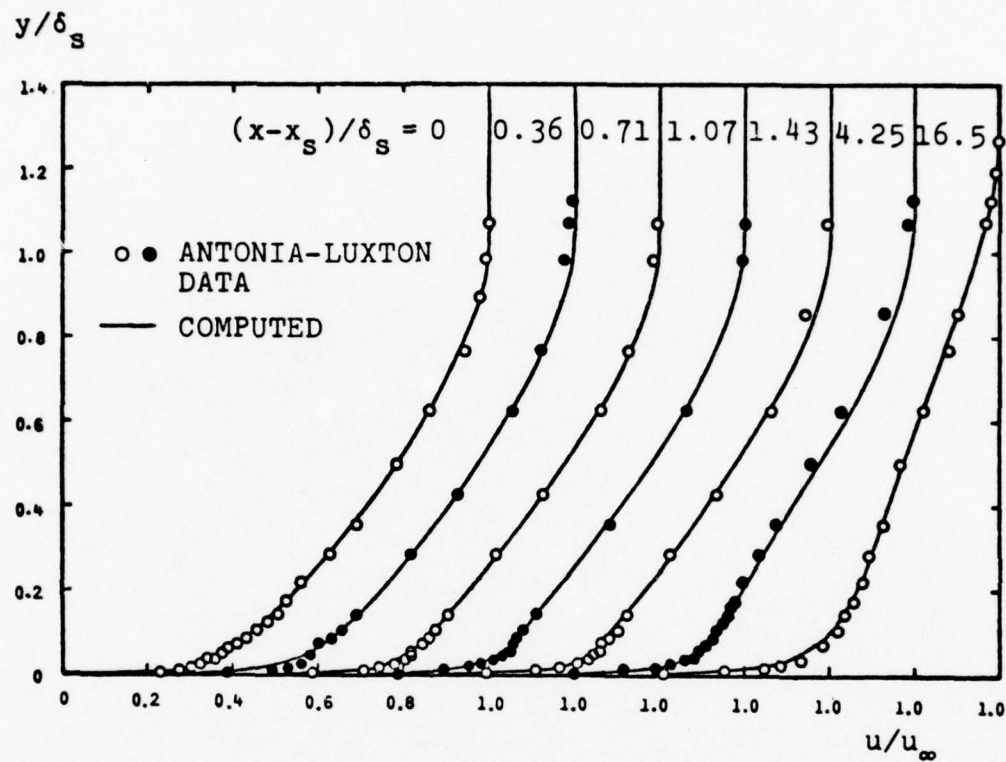


Figure 17. Comparison of computed and measured velocity profiles for a turbulent boundary layer subjected to a sudden change in surface roughness; $U_\infty \delta_s / \nu = 2.6 \cdot 10^4$.

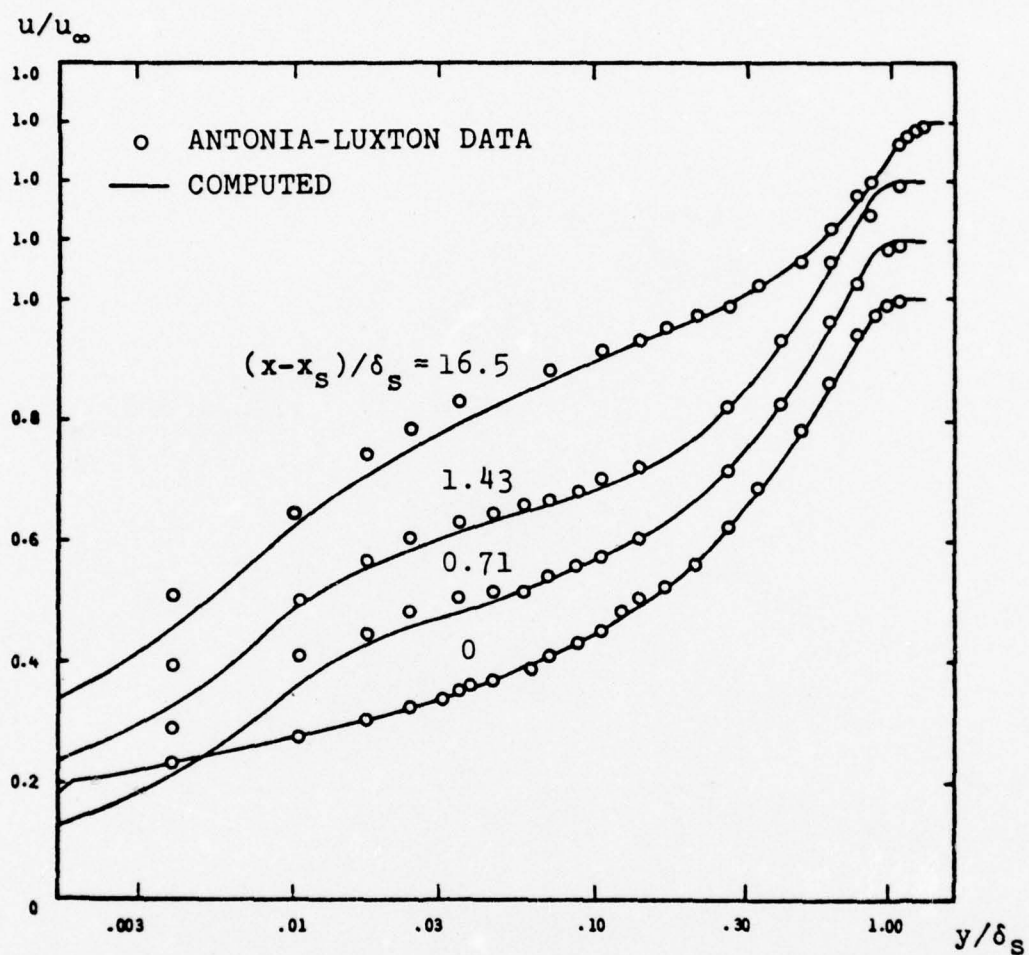


Figure 18. Comparison of computed and measured velocity profiles for a turbulent boundary layer subjected to a sudden change in surface roughness; $U_\infty \delta_S / \nu = 2.6 \cdot 10^4$.

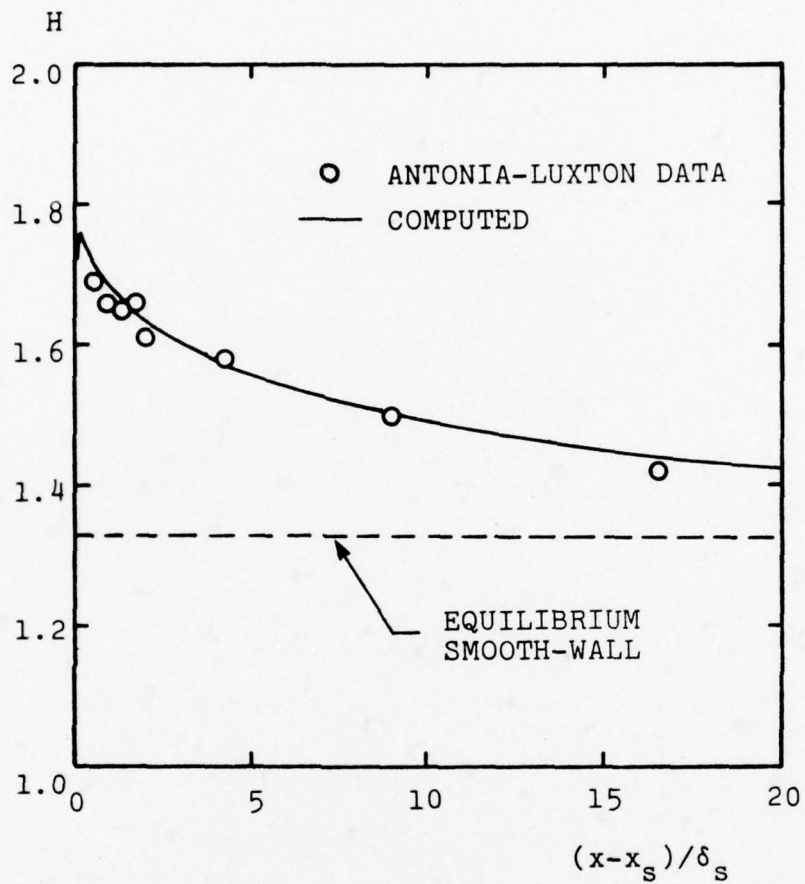


Figure 19. Comparison of computed and measured shape factor for a turbulent boundary layer subjected to a sudden change in surface roughness; $U_\infty \delta_s / \nu = 2.6 \cdot 10^4$.

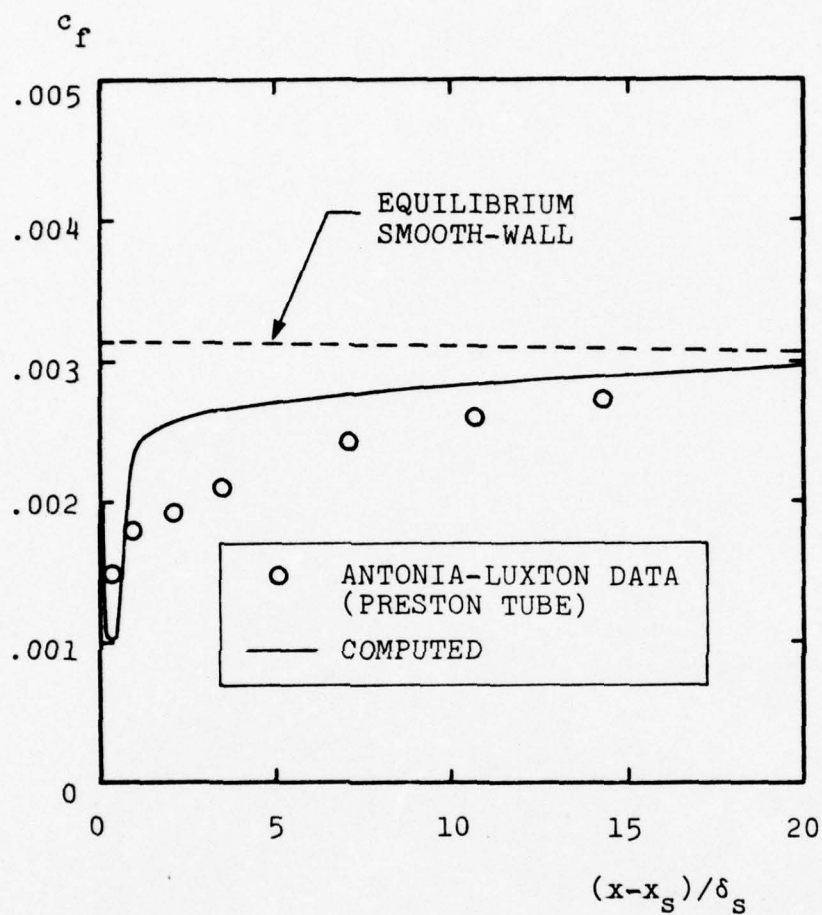


Figure 20. Comparison of computed and measured skin friction for a turbulent boundary layer subjected to a sudden change in surface roughness; $U_\infty \delta_s / \nu = 2.6 \cdot 10^4$.

However, since a rapid initial drop in c_f is generally observed for such a flow, the model's predicting this subtle phenomenon is encouraging.

4. BLUNT-BODY APPLICATIONS

The preceding section presents tests of the turbulence/transition model for well-documented flows, including several effects pertinent to transition on re-entry vehicles. Although the tests are for geometries quite different from re-entry vehicles, the tests (because the flows are well-documented) provide a definitive measure of model accuracy. However, because the primary objective of this study is to devise an accurate method for predicting transition on re-entry vehicle nosetips, additional tests are needed which include the special conditions prevailing for flow past re-entry vehicle geometries. In this section, we hence focus upon re-entry vehicle transition. The section consists of two parts. In the first part (Subsection 4.1), the PANT²⁷ ground-test experiments on roughened spheres are simulated; experimental data are included for comparison. The second part presents results of a series of computations testing the model's ability to predict transition sensitivity to surface roughness, cooling and mass addition; high Mach number; freestream noise and unit Reynolds number; and nonspherical geometry.

4.1 PANT GROUND-TEST EXPERIMENTS

In our first re-entry vehicle application, we simulate the PANT experiments in which a Mach 5 airstream flows past a sphere-cone of nose radius, r_N . All computations are for

$$r_N = 2.5 \text{ inches} \quad (59)$$

while the ratio of surface temperature, T_w , to freestream total temperature, T_{t_∞} , is

$$T_w/T_{t_\infty} = 0.4 \quad (60)$$

Boundary-layer-edge pressure is given by the modified Newtonian pressure distribution; molecular viscosity, μ , is determined from the Sutherland law. Freestream turbulence intensity is assumed to range from about 0.10% to 0.30% so that, consonant with the arguments presented in Appendix A, the turbulent mixing energy at the boundary-layer edge is given by

$$T' = \frac{200}{3} \frac{\sqrt{e_e}}{U_{avg}} = 2\% \quad (61)$$

The turbulence scale at the boundary-layer edge is

$$l_e = .09 \sqrt{\alpha^*} \delta \quad (62)$$

Roughness height, k , varies from 0.1 mil to 100 mils, a much wider range than considered in our prior applications.^{4,5}

Figure 21 compares computed and measured transition location with PANT measurements; the PANT correlation²⁸ is also shown for reference. Consistent with the data, model predictions show that the PANT curve provides a reasonably good correlation for $(kT_e/\theta T_w)_t$ between about 1 and 10. Similar to the measured trend, the computed Re_{θ_t} asymptotes to a constant value for both small and large roughness heights. Figure 22 shows computed incipient transition unit Reynolds number, Re_{∞_1} , as a function of k ; by definition, Re_{∞_1} is the unit Reynolds number below which transition occurs downstream of the sonic point. Computed values of Re_{∞_1} are close to corresponding measured values.²⁷

4.2 OTHER TEST CASES

To test the model's ability to predict transition sensitivity to the various phenomena affecting nosetip transition, further test computations have been made. Experimental data sources were unavailable to the authors at the time the computations

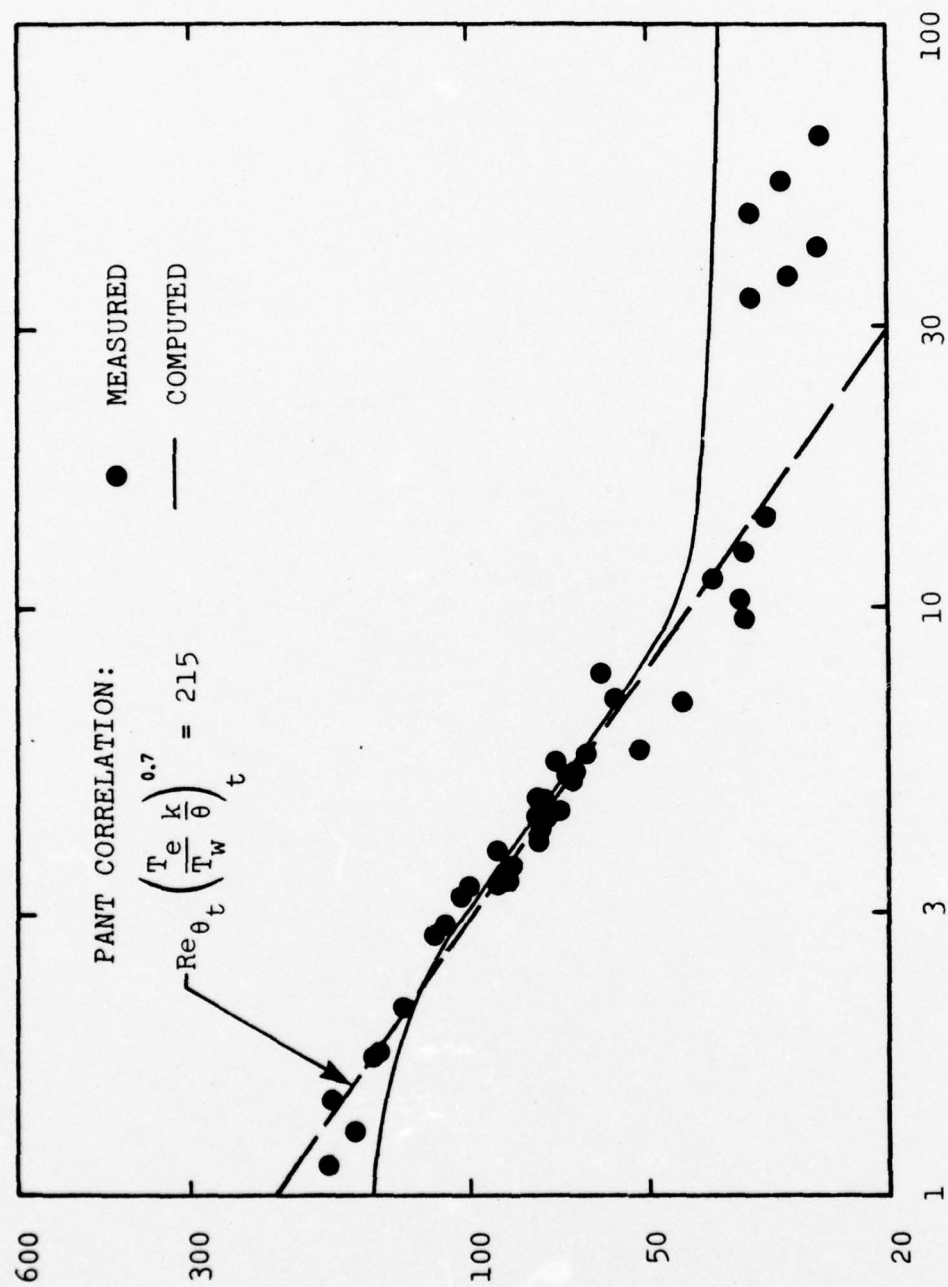


Figure 21. Comparison of computed and measured transition Reynolds number for the PANT wind tunnel experiments.

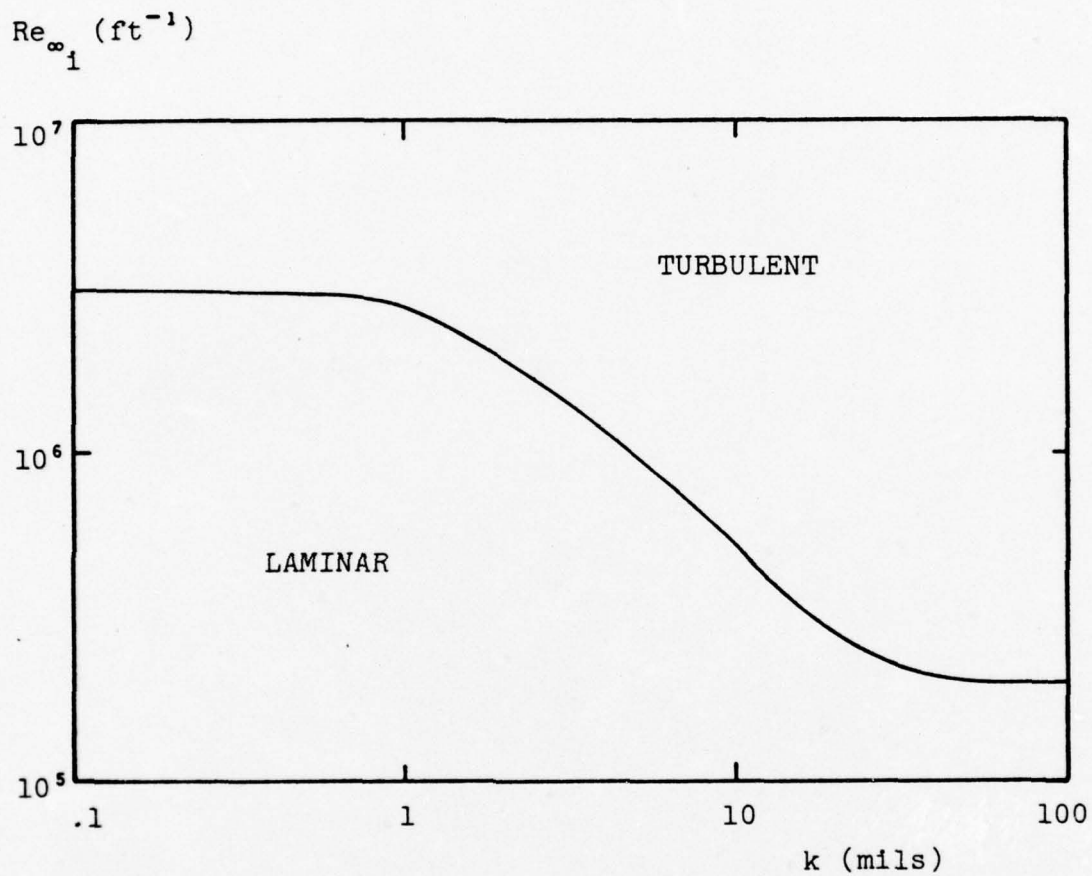


Figure 22. Computed incipient transition unit Reynolds number; $M_{\infty} = 5$, $T_w/T_{t_{\infty}} = 0.4$.

were performed. Table 2 summarizes the various test computations; with the exception of Case 8 (see Appendix B), all of the test cases are for spherical bodies. For each case, a transition prediction has been made; then, the change in the value of the "primary variable" required to change the transition state (i.e., laminar to turbulent or turbulent to laminar) has been determined (provided such a change is possible).

Subsections 4.2.1 through 4.2.6 present results of the computations; the concluding subsection summarizes the results. With the exception of freestream turbulence intensity and scale and pressure distributions, all input data are as defined in Table 2 and Appendix B. All cases use the modified Newtonian pressure distribution while the boundary-layer-edge value of the turbulence scale, l , is given by Equation (62). The free-stream turbulence intensity varies from case to case. Small values ($\sim 0.01\%$) are used for flight-test cases. Larger values ($\sim 1\%$) as defined in Figure B1 of Appendix B are used for ground-test cases.

4.2.1 Combined Effects of Roughness, Cooling and Mass Addition

We begin with Test Cases 1 through 3 which are clearly ground-test experiments. The working fluid is air with constant specific heat ratio $\gamma = 1.4$; viscosity is given by Sutherland's law. The only assumed input datum is boundary-layer-edge turbulence intensity. From Figure B1 of Appendix B, the value of $100\sqrt{\langle u_e'^2 \rangle}/U_e$ is found to be 0.75% , wherefore we assume

$$T' = 0.75\% \quad (63)$$

where U_{avg} is defined in Appendix A.

Table 3 summarizes results of the computations. As shown, for the baseline case in which $k = 5$ mils, $B' = 0.6$ and $T_w/T_{t_\infty} = 0.6$,

Table 2. Blunt-Body Test Cases[†]

Case Number	Effect Analyzed	Input Conditions	Primary Variable
1	Combined effects of surface roughness, wall cooling and mass addition	$p_{t\infty} = 220$ psia, $T_{t\infty} = 850^\circ\text{R}$ $M_\infty = 6$, $r_N = 7''$ $k = 5$ mils, $B' = 0.6$ $T_w/T_{t\infty} = 0.6$	k
2	Same as 1	Same as 1	B'
3	Same as 1	Same as 1	$T_w/T_{t\infty}$
4	High Mach number combined effects of surface roughness, wall cooling and mass addition	Flight trajectory in Table B1 of Appendix B. Altitude = 50 kft $r_N = 0.75''$, $k = 0.4$ mil	Altitude
5	Same as 4	Same as 4 except $k = 15$ mils, non-sandgrain roughness with $L/k = 5$	Altitude
6	Freestream noise and unit Reynolds number effects	$p_{t\infty} = 260$ psia, $T_{t\infty} = 850^\circ\text{R}$ $M_\infty = 6$, $r_N = 7''$ $k = 5$ mils, $B' = 0$ $T_w/T_{t\infty} = 1$	$p_{t\infty}$ and freestream turbulence intensity in Figure B1 of Appendix B.
7	Surface mass addition effects	$p_{t\infty} = 220$ psia, $T_{t\infty} = 850^\circ\text{R}$ $M_\infty = 6$, $r_N = 7''$ $k = 0$, $B' = 0.6$ $T_w/T_{t\infty} = 1$	B'
8	Nonspherical shape effects	Same as 1, except laminar stable shape as given in Table B2 of Appendix B.	k
9	Roughness effects for small k/θ	$p_\infty = 0.7$ atm, $T_\infty = 495^\circ\text{R}$ $M_\infty = 3.14$, $r_N = 6.5''$ $k = .01$ mil, $B' = 0$ $T_w/T_{t\infty} = 0.6$	k
10	Same as 9	$p_\infty = 0.77$ atm, $T_\infty = 517^\circ\text{R}$ $M_\infty = 2.73$, $r_N = 4''$ $k = .02$ mil, $B' = 0$ $T_w/T_{t\infty} = 0.75$	k

[†] In all but Case 8, the body is a sphere; B' is the blowing parameter defined by $B' = \rho_w v_w / (\rho_e U_e C_H)$ where C_H is Stanton number; in Case 5, L is peak-to-peak distance between roughness elements.

transition occurs very close to the stagnation point, viz, at an azimuthal angle of 13.8°. The predicted transition coordinates are

$$Re_{\theta_t} = 87 \quad (64)$$

$$\frac{k}{\theta_t}/\psi = 3.10 \quad (65)$$

where ψ is Anderson's²⁸ modified temperature ratio defined by

$$\psi = B'/10 + (1 + B'/4)T_w/T_e \quad (66)$$

These coordinates are very close to the values predicted by the PANT correlation as modified by Anderson for effects of mass addition.

Table 3. Summary of Computation for Test Cases 1 Through 3

Test Case No.	k(mils)	B'	$\frac{T_w}{T_{t\infty}}$	$\frac{s_t}{r_N}$	$\phi_t(^{\circ})$	M_{e_t}	Re_{θ_t}	$\frac{k}{\theta_t}/\frac{T_w}{T_e}$	$\frac{k}{\theta_t}/\psi$
1	5	.6	0.6	.240	13.8	0.30	87	3.87	3.10
↓	2	↓	↓	.503	28.8	0.73	193	1.29	1.04
	1			.600	34.4	0.80	207	0.62	0.50
	1/2			.600	34.4	0.80	207	0.31	0.25
↓	0	↓	↓	.612	35.1	0.82	211	0.00	0.00
2	5	0	0.6	.264	15.1	0.33	84	4.40	4.40
3	5	.6	0.8	.348	19.9	0.44	115	3.01	2.55
↓	↓	↓	0.9	.408	23.4	0.52	128	2.71	2.23
			1.0	.444	25.4	0.52	153	2.17	1.80
			1.5	.600	34.4	0.80	132	1.94	1.64
↓	↓	↓	2.0	.756	43.3	1.06	99	1.97	1.68

The objective of the Test Cases is to individually vary k , B' , and T_w/T_{t_∞} and to determine if variation of these parameters can prevent transition from occurring ahead of the sonic point. Varying k , B' and T_w/T_{t_∞} leads to the following conclusions:

1. It is not possible to change the state of the boundary layer from turbulent to laminar by decreasing roughness height. Even in the perfectly smooth case ($k=0$), transition occurs just ahead of the sonic point.
2. Transition occurs for all blowing rates, including the unblown case ($B'=0$).
3. T_w/T_{t_∞} must be increased to 2.0 to cause transition to occur beyond the sonic point.

4.2.2 High Mach Number Combined Effects of Roughness, Cooling and Mass Addition

Turning now to Test Cases 4 and 5, we test the model under flight-test conditions. In the computations, we take account of high-temperature properties of air by assuming the working fluid to be a perfect gas with constant specific heat ratio $\gamma=1.2$; viscosity is given by

$$\mu = 2.518 \cdot 10^{-10} T + 4.193 \cdot 10^{-7} \text{ lb} \cdot \text{sec}/\text{ft}^2 \quad (67)$$

where T is temperature in degrees Rankine. All other input are as defined in Appendix B.

Two freestream turbulence intensities, $T'_\infty = .01\%$ and $.03\%$ are considered. Table 4 summarizes results of the computations, including inferred values of the boundary-layer-edge intensity (Appendix A).

For a roughness height of 0.4 mils (Test Case 4) and for turbulence intensities of $.01\%$ and $.03\%$, no transition occurs at 50.2 kft. Decreasing altitude fails to induce transition

Table 4. Summary of Computations for
Test Cases 4 and 5

Test Case No.	Altitude (kft)	$T'_{\infty}(\%)$	$T'(\%)$	$\frac{s_t}{r_N}$	$\phi_t(^{\circ})$	M_{e_t}	Re_{θ_t}	$\frac{k}{\theta_t} \frac{T_w}{T_e}$	$\frac{k}{\theta_t} / \psi$
4 ↓	50.2	.010	.117	← Laminar →					
	37.7	↓	.121	← Laminar →					
	50.2	.030	.351	← Laminar →					
	43.8	↓	.359	← Laminar →					
	40.7	↓	.362	.624	35.8	0.87	182	2.15	1.74
	37.7	↓	.363	.540	30.9	0.74	169	2.43	1.99
5 ↓	50.2	.010	.117	.162	9.3	0.22	43	88.6	71.9
	63.7	↓	.112	.252	14.4	0.34	50	67.0	50.9
	81.1	↓	.105	.624	35.8	0.87	78	36.3	27.5
	84.7	↓	.104	← Laminar →					
	50.2	.030	.351	.156	8.9	0.21	42	88.5	69.0
	81.1	↓	.315	.600	34.4	0.84	75	37.1	28.1
	84.7	↓	.312	← Laminar →					
5 (with $e_w=0$) ↓	50.2	.010	.117	← Laminar →					
	37.7	↓	.121	← Laminar →					
	50.2	.030	.351	.528	30.3	0.73	134	74.0	58.0
	53.5	↓	.348	.612	35.1	0.86	142	64.6	50.3
	56.9	↓	.345	.696	39.9	0.99	152	57.0	44.1
	60.2	↓	.342	← Laminar →					

even at 37.7 kft when freestream intensity is .01%. However, when .03% freestream turbulence intensity is used, transition first occurs at 40.7 kft.

For $k=15$ mils (Test Case 5), computations have been performed two ways. First, the computations make no special allowance for the fact that the roughness is non-sandgrain; then, computations have been performed with surface-generated turbulence

fluctuations suppressed as a first approximation to simulating distributed roughness; to do this, we replace the first of Equations (51) by

$$e = 0 \quad \text{at} \quad y = 0 \quad (68)$$

The following results have been obtained:

No Allowance for Non-Sandgrain Roughness

Transition occurs at 50.2 kft for freestream intensities of .01% and .03%. For both intensities, altitude must be increased to 84.7 kft in order to change the state of the boundary layer, i.e., to cause transition to occur beyond the sonic point.

Surface Disturbances Suppressed

When freestream intensity is .01% the flow is laminar at 50.2 kft; for .03% freestream turbulence, transition occurs at 50.2 kft. Thus for $T'_{\infty} = .01\%$ we decrease altitude to see if the boundary layer will transist; however, the flow remains laminar all the way down to 37.7 kft. By contrast, we increase altitude for $T'_{\infty} = .03\%$ to determine the altitude at which the boundary layer remains laminar ahead of the sonic point; inspection of Table 4 shows that no transition occurs at altitudes greater than 60.2 kft.

Measurements²⁹ indicate that the vehicles considered in Test Cases 4 and 5 transist at nearly the same altitude. Although the Test Case 5 vehicle transists at a higher altitude than that of Test Case 4, the discrepancy has been greatly reduced by using Equation (68). Hence, suppressing surface-generated disturbances appears appropriate for analytically simulating non-sandgrain roughness.

4.2.3 Freestream Noise and Unit Reynolds Number

For Test Case 6, computations have been performed for the five values of $p_{t\infty}$ at which $\sqrt{\langle u_e'^2 \rangle}/U_e$ is given in Figure B1 of Appendix B, viz, 260, 210, 170, 130, and 90 psia. As indicated in Table 2, this test case has neither mass addition nor heat transfer; by varying $p_{t\infty}$, we vary only the freestream unit Reynolds number. Table 5 presents results of the computations; as shown, transition occurs at $\phi_t = 21.3^\circ$ for the baseline case, $p_{t\infty} = 260$ psia; total pressure must be reduced to 130 psia to achieve laminar flow.

Table 5. Summary of Computations for Test Case 6

$p_{t\infty}$ (psia)	$10^{-6} Re_\infty$ (ft $^{-1}$)	$T'(\%)$	$\frac{s_t}{r_N}$	$\phi_t(^{\circ})$	M_{e_t}	Re_{θ_t}	$\frac{k}{\theta_t} \frac{T_w}{T_e}$
260	5.47	0.91	.372	21.3	0.47	112	3.37
210	4.06	0.83	.516	29.6	0.67	133	2.59
170	3.29	0.76	.720	41.3	0.99	156	1.94
130	2.52	0.79	← Laminar →				
90	1.74	0.88	← Laminar →				

4.2.4 Surface Mass Addition

For Test Case 7, we isolate the effect of surface mass addition on nosetip transition under ground-test conditions. As in the preceding test case, we have no heat transfer; in addition, the nosetip is perfectly smooth ($k = 0$). From Figure B1 of Appendix B, the boundary-layer-edge turbulence intensity is 0.75%. For the baseline case ($B' = 0.6$), transition occurs very close to the sonic point (see Table 6). Decreasing B' causes only a slight downstream movement of the transition point, asymptoting to $M_{e_t} = 1.40$ in the nonblown ($B' = 0$) case.

Table 6. Summary of Computations for Test Case 7

B'	$\frac{s_t}{r_N}$	$\phi_t(^{\circ})$	M_{e_t}	Re_{θ_t}
0.60	.732	41.9	1.02	232
0.40	.780	44.7	1.10	226
0.10	.900	51.6	1.35	213
0.01	.924	52.9	1.40	205
0.00	.924	52.9	1.40	205

4.2.5 Nonspherical Shape

To obtain a measure of model-predicted effects of body geometry, Test Case 8 considers the laminar-stable-shape configuration (Appendix B). All flow conditions match those of the Test Case 1 computations. For $k=5$ mils, transition occurs at $s_t/r_N = .280$, a bit further downstream than for the spherical body considered in Test Case 1. Table 7 summarizes results obtained as roughness height decreases to zero; Figure 23 compares predicted transition location for the laminar stable shape with that obtained for a sphere. Decreasing the roughness height to $k=1$ mil is sufficient to move transition to a point just downstream of the sonic point; further decrease of k causes no change in transition point location.

Table 7. Summary of Computations for Test Case 8

k(mils)	$\frac{s_t}{r_N}$	M_{e_t}	Re_{θ_t}	$\frac{k}{\theta_t} \frac{T_w}{T_e}$	$\frac{k}{\theta_t} / \psi$
5	.280	0.36	107	3.65	2.93
1	.693	1.08	373	0.35	0.28
1/2	.693	1.08	352	0.18	0.15
1/200	.693	1.08	339	0.0019	0.0015
0	.693	1.08	339	0	0

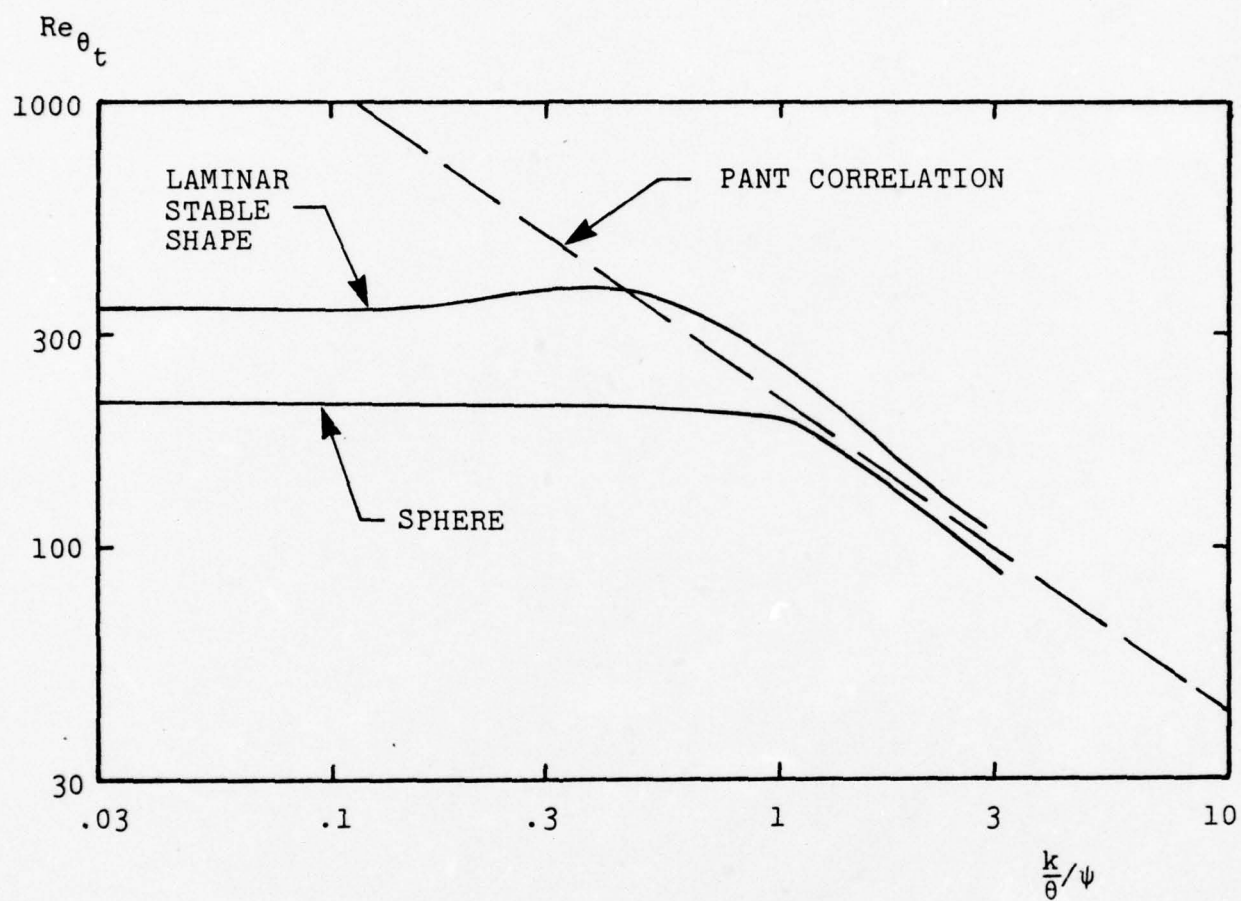


Figure 23. Comparison of computed effects of surface roughness on transition location for the laminar stable shape and a sphere.

4.2.6 Roughness Effects for Small k/θ

The final round of applications (Test Cases 9 and 10) tests the model's accuracy for nosetip transition in the limit of small roughness height. Both test cases are for vehicles in free flight; Test Case 9 simulates the experiments of Buglia³⁰ while Test Case 10 corresponds to the measurements of Hall, Speegle and Piland.³¹ Because the Mach numbers for both cases fall in the supersonic (rather than the high hypersonic) range, the working fluid is assumed to be air with $\gamma = 1.4$ and μ given by Sutherland's law. Freestream turbulence level is assumed to be .01% so that according to Appendix A,

$$T' = \begin{cases} .088\% & , \text{ Test Case 9} \\ .084\% & , \text{ Test Case 10} \end{cases} \quad (69)$$

For Test Case 9, a roughness height of .01 mil causes transition just ahead of the sonic point (see Table 8). At transition, the predicted s_t/r_N is .698; by comparison, Buglia's measurements indicate that s_t/r_N lies between 0.66 and 0.78. Decreasing k causes only a slight movement of the transition point; for the perfectly smooth case, transition occurs closer to, but still upstream of the sonic point.

Table 8. Summary of Computations for Test Cases 9 and 10

Test Case No.	k(mils)	$\frac{s_t}{r_N}$	$\phi_t(^{\circ})$	M_{e_t}	Re_{θ_t}	$\frac{k}{\theta_t} \frac{T_w}{T_e}$
9 ↓	.010	.698	40.0	0.94	654	.0218
	.003	.711	40.7	0.96	664	.0065
	.001	.711	40.7	0.96	665	.0022
	0	.711	40.7	0.96	666	0
10 ↓	.020	—	> 65	—	—	—
	.295	1.128	64.6	1.839	667	.326
	.300	1.044	59.8	1.627	552	.421

For Test Case 10, the flow is laminar up to 65° from the centerline when $k = .02$ mil. We are unable to integrate beyond $\phi = 65^\circ$ because the Newtonian pressure distribution fails to provide an accurate approximation for larger values of ϕ . Since Hall, Speegle and Piland measure transition at an azimuthal angle between about 75° and 90° , we are thus unable to make a definitive prediction for Test Case 10. However, some insight can be gained by using larger roughness heights. Computations for $k = .295$ mil and $k = .300$ mil indicate that transition may occur with $k = .02$ mil at a point downstream of $\phi = 65^\circ$. That is, transition occurs with

$$\left. \begin{aligned} \frac{k}{\theta_t} \frac{T_w}{T_e} &= .326 \quad , \quad Re_{\theta_t} = 667 \quad \text{for } k = .295 \text{ mil} \\ \frac{k}{\theta_t} \frac{T_w}{T_e} &= .421 \quad , \quad Re_{\theta_t} = 552 \quad \text{for } k = .300 \text{ mil} \end{aligned} \right\} \quad (70)$$

These points are close to the PANT correlation. However, we know the model predicts a finite asymptotic value for Re_{θ_t} as $k/\theta_t \rightarrow 0$. This asymptote thus occurs for $Re_{\theta_t} > 667$, and hence for $\phi_t > 65^\circ$. To predict the transition point, the computation would have to be repeated using a more accurate pressure distribution.

4.2.7 Summary

Based on the results obtained for the PANT simulations of Subsection 4.1 and for the ten test cases, several general observations can be made.

First, over a very wide range of roughness scale heights, increasing k destabilizes a nosetip boundary layer. However, the change in the boundary layer's stability characteristics is most pronounced for a narrow range of roughness heights, viz, $0.5 \leq \frac{k}{\theta_t} / \psi \leq 10$. In this range, Re_{θ_t} varies by an order

of magnitude. Outside this range, transition is much less sensitive to variations in roughness. For example, as illustrated in the PANT simulations and in Test Cases 1, 9 and 10, when roughness height decreases to very small values, the transition point eventually becomes insensitive to roughness and Re_{θ_t} is independent of k ; in the limit $k/\theta \rightarrow 0$ transition location depends strongly upon freestream turbulence intensity. Similarly, for very large roughness height, Re_{θ_t} and s_t/r_N asymptote to constant values signifying the approach to a completely roughness dominated regime; freestream disturbances are unimportant in this regime. Computations for Test Case 5 show that transition induced by sandgrain roughness is quite different from that induced by non-sandgrain, distributed type roughness. The primary difference in physical mechanisms active for these two kinds of roughness is in the magnitude of surface fluctuations generated by the roughness elements. For sandgrain roughness, local flow separations give rise to strong fluctuations near the surface; by contrast, for distributed, widely-spaced roughness elements, separation will be more orderly and less likely to cause random, turbulence-like fluctuations near the surface.

Second, the strong curvature on the laminar stable shape tends to make the velocity profile more stable. As shown in Figure 23, Re_{θ_t} is consistently higher at all roughness heights for the laminar stable shape than for a sphere.

Third, as illustrated in Test Case 3, cooling destabilizes a rough-wall boundary layer. The destabilization occurs because cooling thins the boundary layer wherefore k/θ increases. This increase in k/θ makes the surface appear rougher so that Re_{θ_t} decreases. Test Case 2 shows that surface mass addition has a relatively weak effect on a rough-wall boundary layer under ground-test conditions. The computations fail to

illustrate an interesting possibility, viz, that combined blowing and cooling may cancel each other's effect on boundary-layer stability. That is, because blowing thickens the boundary layer while cooling has a thinning effect, a unique combination of blowing and cooling may permit a constant k/θ and consequently a fixed transition point.

Fourth, all of the first three points should be valid for the freestream noise environment specified in Figure B1 of Appendix B. In fact, this relatively noisy environment is responsible for the relative insensitivity of Re_{θ_t} to roughness and mass addition observed in Test Cases 1 and 2. In both cases the boundary layer could not be stabilized by any change in k or B' . The limiting $k/\theta \rightarrow 0$ value of Re_{θ_t} , a limiting value strongly controlled by freestream noise, is achieved at finite values of k/θ and B' ; thus, the effectiveness of roughness and mass addition is inhibited by freestream noise.

Fifth, the first four conclusions are expected to hold for the range of freestream Mach numbers from 2 to 20. However, results of Test Cases 4 and 5 suggest that nontrivial departures from the PANT correlation may occur at Mach 20.

5. DISCUSSION

Results presented in Sections 3 and 4 demonstrate the value of the turbulence-model transition-prediction method. While the program objective has been to devise an accurate and efficient method for predicting transition on re-entry vehicle nosetips, we have been successful in predicting transition for other aerodynamic geometries as well. The model's representing more than one class of flows provides hope that a universally applicable transition-prediction method has been devised.

Results for the smooth-wall, incompressible FPBL illustrate an encouraging aspect of the model. With no transition-specific modifications to the basic turbulence model aside from the argument used to set the value of the closure coefficient λ [Equation (23)], many features of FPBL transition are accurately predicted including transition sensitivity to free-stream turbulence intensity, transition width, skin-friction overshoot, and transitional velocity profiles. In addition, aside from boundary-condition modifications introduced for numerical reasons, the model naturally simulates transition sensitivity to surface roughness and surface mass addition.

A primary limitation of the theory is its inability to simulate spectral effects. The closure coefficients in the model equations are essentially correlation coefficients which have been integrated over the turbulent spectrum. Hence, as discussed in Subsection 2.3 we must introduce transition-specific modifications in order to accurately predict transition sensitivity to phenomena which reduce the range of unstable frequencies such as pressure gradient, suction, and surface heat transfer. Nevertheless, because of their close tie to linear-stability

theory, the modifications proposed in Subsection 2.3 enhance the model's credibility relative to earlier versions of the model.

Specific areas in which further model development and validation would be beneficial include the following: (a) surface disturbances emanating from injected mass, (b) differences between sandgrain and non-sandgrain roughness, and (c) turbulence spectrum. In devising the surface boundary conditions for surfaces with mass addition, we have assumed the injected gas to be free of turbulent fluctuations. This is probably inaccurate for materials with high ablation rates, and some account of surface disturbances should be made in such applications. Similarly, surface disturbances generated by roughness elements depend upon peak-to-peak distance, L , between roughness elements as well as upon peak-to-valley distance, k . Our rough-surface boundary conditions are designed primarily for sandgrain roughness which is the special limiting case in which $L/k \sim O(1)$. Because many materials ablate with a range of L to k ratios, further development of the rough-surface boundary conditions is needed. Finally, the model masks many of the subtle wave amplification and distortion processes occurring during transition, processes which are strongly spectrum dependent. The model's credibility would be enhanced considerably if some direct account of spectral effects were included.

In conclusion, within the bounds of the limitations noted above, the model is ready for general engineering applications including flight-test cases. Based on results obtained in this two-and-one-half year project, we expect that future applications will substantiate this claim.

APPENDIX A

BOUNDARY-LAYER-EDGE TURBULENCE INTENSITY FOR RE-ENTRY VEHICLE NOSETIPS

To determine the turbulence intensity at the boundary-layer edge, T' , for re-entry vehicle nosetips, we must account for two effects:

1. Turbulence amplification near the stagnation streamline caused by the uniform straining region between the freestream and the boundary-layer edge.
2. Variations in T' attending rapid acceleration of the fluid away from the stagnation point.

The first effect is pertinent when only the freestream intensity, T'_∞ , is known. The second effect requires special attention here because, for simplicity, we use a constant average value for T' in all computations; accounting for the second effect permits evaluation of an appropriate average value. This appendix presents the method used to account for these two effects.

In all of the blunt-body computations of Section 4, T'_∞ is defined in terms of the streamwise fluctuating velocity, u'_∞ , as follows:

$$T'_\infty = 100\sqrt{\langle u'^2_\infty \rangle}/U_\infty \quad (A1)$$

Since the flow is normal to the body, the definition of e [Equation (12)] implies that

$$T'_\infty = \frac{200}{3} \frac{e_\infty^{1/2}}{U_\infty} \quad (A2)$$

Similarly, T' and e_e are related as follows

$$T' = \frac{200}{3} \frac{e_e^{\frac{1}{2}}}{U_e} \quad (A3)$$

Therefore,

$$\frac{T'}{T'_\infty} = \left(\frac{e_e}{e_\infty} \right)^{\frac{1}{2}} \frac{U_\infty}{U_e} \quad (A4)$$

As shown by Traci and Wilcox,³² the ratio of e_e to e_∞ on the stagnation streamline primarily depends on Reynolds number. Figure A1 shows the predicted variation of e_e/e_∞ as a function of Reynolds number based on nose radius, Re_{r_N} .

As noted above, it is convenient to assume T' is constant throughout the nosetip region. This is not rigorously correct, however, since U_e varies with x while e_e probably changes only slightly as x increases. Thus, some average value of T' must be devised in order to achieve a meaningful prediction. The average value used in this study is given by

$$\frac{T'}{T'_\infty} = \left(\frac{e_e}{e_\infty} \right)^{\frac{1}{2}}_{x=0} \frac{U_\infty}{U_{avg}} \quad (A5)$$

where U_{avg} is the average velocity between the stagnation point ($x=0$) and the sonic point ($x=x^*$), defined by

$$U_{avg} = \frac{1}{x^*} \int_0^{x^*} U_e dx = \frac{1}{2} U_e^* \quad (A6)$$

where U_e^* is velocity at the sonic point. The integral in Equation (A6) has been evaluated by noting that U_e increases approximately linearly with x . Finally, to relate U_e^* and U_∞ , we use the fact that total temperature is constant along the boundary-layer edge wherefore

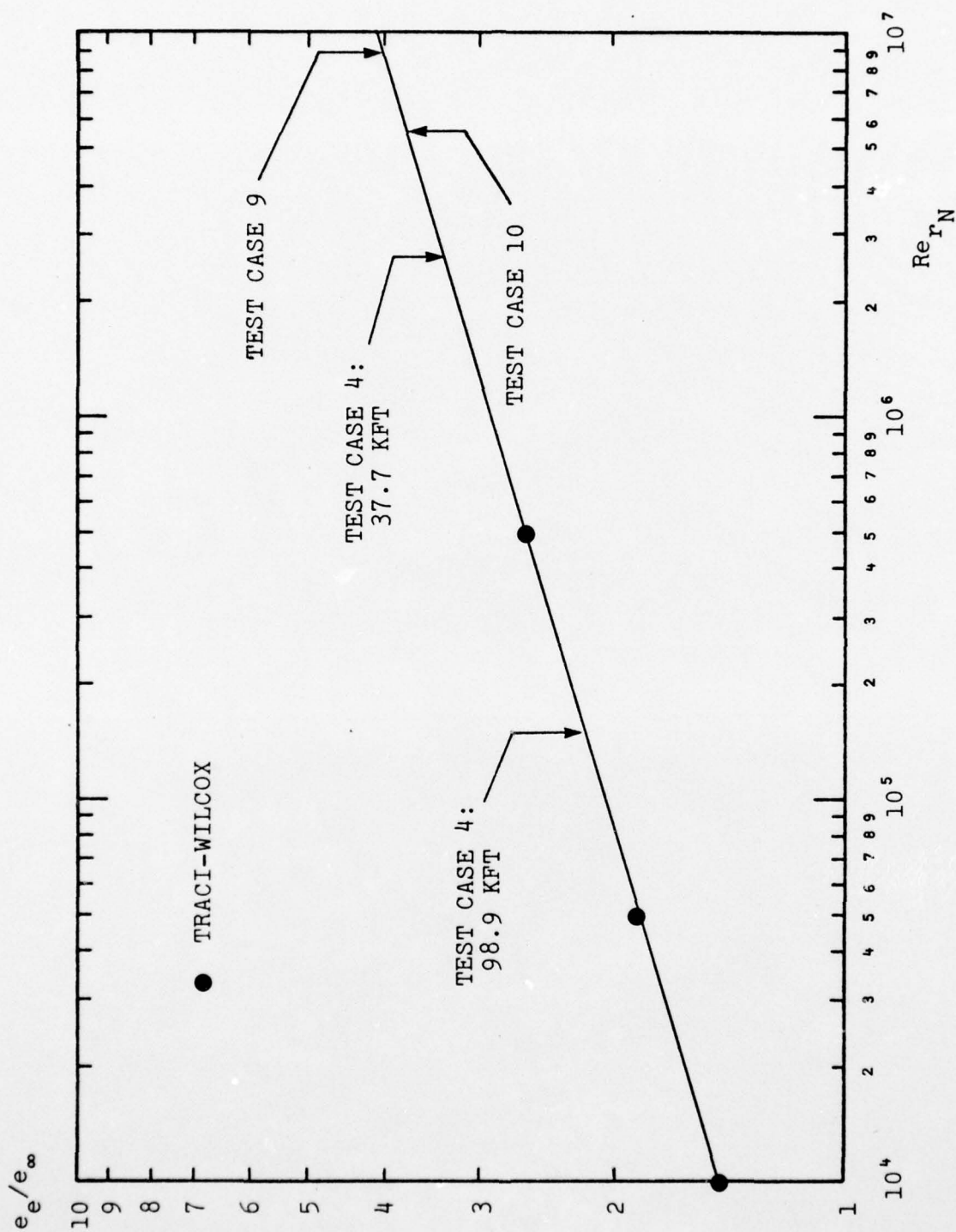


Figure A1. Stagnation region amplification of turbulent mixing energy as a function of nose-radius Reynolds number.

$$\left(\frac{U_e^*}{U_\infty}\right)^2 = \frac{\gamma-1}{\gamma+1} \left[1 + \frac{2}{(\gamma-1)M_\infty^2}\right] \quad (A7)$$

Combining Equations (A5-A7) yields the desired relation between T' and T'_∞ , viz,

$$\frac{T'}{T'_\infty} = 2 \sqrt{\frac{\gamma+1}{\gamma-1} \left(\frac{e_e}{e_\infty}\right)_{x=0} \left[1 + \frac{2}{(\gamma-1)M_\infty^2}\right]^{-1}} \quad (A8)$$

where $(e_e/e_\infty)_{x=0}$ is given in Figure A1 as a function of Re_{r_N} .

APPENDIX B

INPUT DATA FOR BLUNT-BODY TEST CASES

Figure B1 and Tables B1 and B2 define pertinent input data for the blunt-body test cases of Subsection 4.2. The quantity B' is the blowing parameter defined by

$$B' = \frac{\rho_w v_w}{\rho_e U_e C_H}$$

where C_H is Stanton number.

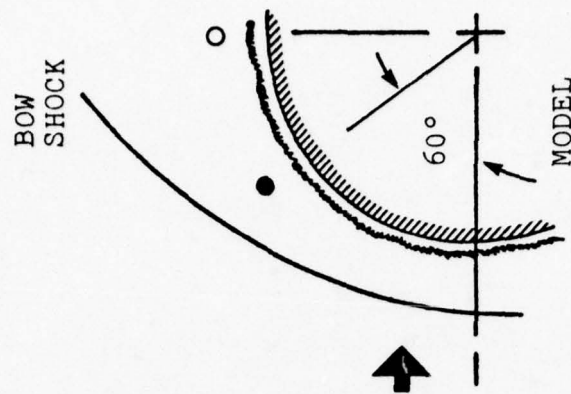
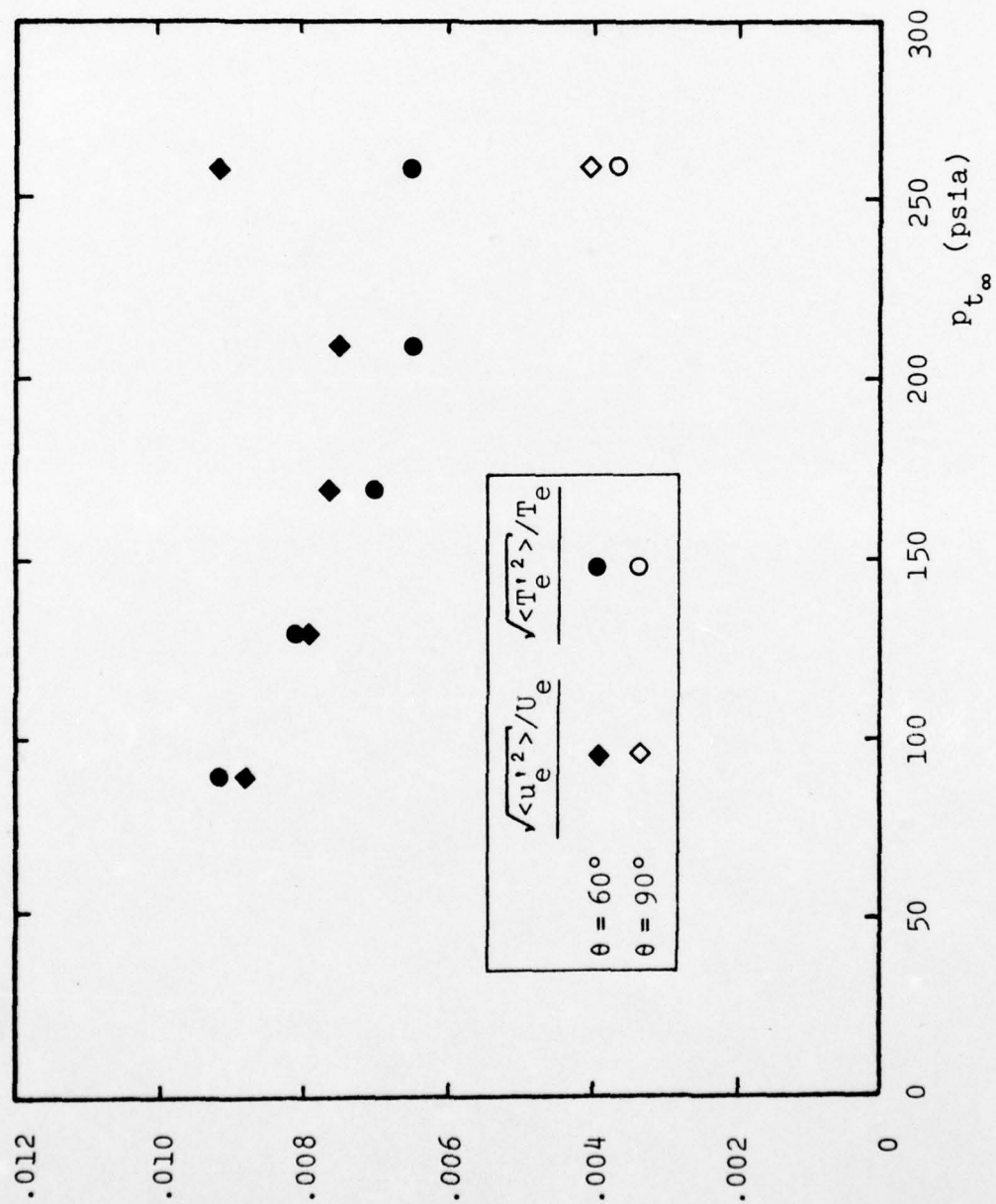


Figure B1. Shock layer disturbance levels.

Table B1. Flight Trajectory Variables for Cases 4 and 5

Altitude (ft)	Velocity (ft/sec)	Stagnation Enthalpy (BTU/lb)	Freestream Density (lb/ft ³)	P _{t2} (atm)	B'	T _w (°R)	H _w /H _{t∞}
98901	22880	10456	.00105	8.07	.69*	7082	.45
95338	22851	10430	.00130	9.97	.76	7142	.46
91778	22814	10397	.00154	11.8	.71	7191	.47
88222	22771	10357	.00186	14.2	.71	7244	.48
84678	22718	10309	.00221	16.7	.72	7290	.48
81138	22653	10250	.00260	19.6	.72	7335	.48
77611	22573	10178	.00310	23.2	.72	7383	.49
74098	22476	10091	.00368	27.3	.72	7428	.49
70597	22359	9986	.00448	32.9	.72	7480	.50
67119	22213	9856	.00519	37.6	.72	7516	.50
63668	22037	9700	.00611	43.6	.71	7555	.51
60243	21821	9511	.00719	50.3	.70	7591	.52
56857	21550	9276	.00846	57.7	.69	7623	.52
53517	21234	9006	.00986	65.3	.67	7650	.53
50226	20879	8708	.0116	74.3	.65	7676	.54
46998	20485	8382	.0135	83.2	.63	7696	.55
43829	20049	8024	.0157	92.7	.60	7712	.56
40732	19572	7652	.0182	102	.57	7721	.57
37713	19056	7254	.0210	112	.54	7727	.58

* To a good approximation, B' may be considered to be constant over the spherical nosetip at a given altitude.

Table B2. Laminar Stable Shape Configuration

Running Surface Distance, s^*	Local Body Angle, $\phi(^{\circ})$	Local Body Curvature, $d\phi/ds$	Local Radial Coordinate, r	Local Axial Coordinate, z
0.0	90.	-1.	0.0	0.0
0.025217	88.555	-1.0002	0.025214	0.0003179
0.050049	87.132	-1.0009	0.050028	0.0012524
0.075137	85.692	-1.0022	0.075066	0.0028224
0.10023	84.250	-1.0039	0.10006	0.0050215
0.12506	82.820	-1.0061	0.12473	0.0078172
0.15015	81.372	-1.0089	0.14958	0.011267
0.17523	79.920	-1.0123	0.17433	0.015344
0.20007	78.477	-1.0162	0.19872	0.019998
0.22515	77.013	-1.0209	0.22324	0.025323
0.25024	75.541	-1.0263	0.24761	0.031274
0.27507	74.077	-1.0323	0.27158	0.037780
0.30016	72.588	-1.0393	0.29561	0.044975
0.32525	71.089	-1.0473	0.31945	0.052795
0.35008	69.592	-1.0562	0.34283	0.061148
0.37517	68.067	-1.0665	0.36622	0.070208
0.40000	66.541	-1.0780	0.38913	0.079788
0.42535	64.967	-1.0915	0.41224	0.090195
0.45043	63.387	-1.1067	0.43482	0.10112
0.47501	61.817	-1.1238	0.45664	0.11243
0.50010	60.188	-1.1439	0.47859	0.12459
0.52519	58.527	-1.1674	0.50017	0.13738
0.55027	56.830	-1.1950	0.52137	0.15079
0.57690	54.980	-1.2303	0.54342	0.16571
0.60147	53.221	-1.2698	0.56333	0.18012
0.62605	51.400	-1.3182	0.58278	0.19514
0.65063	49.502	-1.3794	0.60173	0.21079
0.67520	47.505	-1.4591	0.62014	0.22707
0.70183	45.191	-1.5791	0.63940	0.24544
0.72538	42.959	-1.7359	0.65579	0.26235
0.75098	40.220	-2.0227	0.67279	0.28149
0.77504	37.085	-2.6103	0.68784	0.30026
0.80000	31.955	-4.4794	0.70209	0.32074
0.82503	27.348	-2.2723	0.71437	0.34254
0.85005	24.777	-1.4293	0.72532	0.36504
0.87501	23.047	-1.0306	0.73542	0.38786
0.90003	21.746	-0.80111	0.74494	0.41100
0.92506	20.710	-0.65297	0.75400	0.43433
0.95002	19.854	-0.54986	0.76264	0.45775
0.97504	19.123	-0.47370	0.77099	0.48134
1.0	18.488	-0.41545	0.77903	0.50497
1.0250	17.927	-0.36928	0.78685	0.52874
1.0501	17.424	-0.33179	0.79446	0.55264
1.0751	16.972	-0.30098	0.80184	0.57649
1.1000	16.560	-0.27511	0.80904	0.60039
1.1251	16.181	-0.25297	0.81611	0.62446
1.1501	15.833	-0.23401	0.82299	0.64845
1.1750	15.511	-0.21751	0.82973	0.67248
1.2000	15.210	-0.20303	0.83634	0.69655
1.2251	14.928	-0.19016	0.84287	0.72078

* All length variables have been normalized by the stagnation point radius of curvature which is 7.68 in..

REFERENCES

1. Saffman, P.G., "A Model for Inhomogeneous Turbulent Flow," Proc Roy Soc Lond A317, pp 417-433 (1970).
2. Saffman, P.G. and Wilcox, D.C., "Turbulence-Model Predictions for Turbulent Boundary Layers," AIAA Journal, Vol 12, No 4, pp 541-546 (1974).
3. Wilcox, D.C. and Chambers, T.L., "Computation of Turbulent Boundary Layers on Curved Surfaces," DCW Industries Report No DCW-R-07-01 (January 1976).
4. Wilcox, D.C., "Turbulence-Model Transition Predictions for Blunt-Body Flows," AFOSR-TR-74-1714 (July 1974).
5. Wilcox, D.C. and Chambers, T.L., "Further Refinement of the Turbulence-Model Transition-Prediction Technique," AFOSR-TR-75-1682 (July 1975).
6. Wilcox, D.C. and Chambers, T.L., "Effects of Surface Heat Transfer on Boundary-Layer Transition," AFOSR-TR-75-1398 (July 1975).
7. Favre, A.J., "The Equations of Compressible Turbulent Gases," Annual Summary Report No 1, Institute de Mechanique Statistique de la Turbulence (1965).
8. Kolmogorov, A.N., "Equations of Turbulent Motion of an Incompressible Fluid," Izvestia Academy of Sciences, USSR; Physics, Vol 6, Nos 1 and 2, pp 56-58 (1942).
9. Wilcox, D.C. and Alber, I.E., "A Turbulence Model for High Speed Flows," Proceedings of the 1972 Heat Transfer and Fluid Mechanics Institute, Stanford Univ Press, pp 231-252 (1972).
10. Wilcox, D.C. and Traci, R.M., "A Complete Model of Turbulence," AIAA Paper 76-351, San Diego, Calif (July 1976).
11. Laufer, J., "The Structure of Turbulence in Fully Developed Pipe Flow," NACA 1174 (1952).
12. Schlichting, H., Boundary Layer Theory, Fourth Ed, McGraw-Hill, New York, pp 519-527 (1960).
13. Andersen, P.S., Kays, W.M., and Moffat, R.J., "The Turbulent Boundary Layer on a Porous Plate: An Experimental Study of the Fluid Mechanics for Adverse Free-Stream Pressure Gradients," Report No HMT-15, Dept Mech Engr, Stanford Univ, Calif (1972).

14. Schlichting, H., Boundary Layer Theory, Fourth Ed, McGraw-Hill, New York, p 414 (1960).
15. Personal communication between L.M. Mack of JPL and D.C. Wilcox of DCW Industries (February 1976).
16. Crabtree, L.F., "Prediction of Transition in the Boundary Layer on an Aerofoil," Journal Roy Aero Soc, Vol 62, p 525 (1958).
17. Feindt, E.G., "Untersuchungen über die Abhängigkeit des Umschlages Laminar-Turbulent von der Oberflächenrauigkeit und der Druckverteilung," Thesis Braunschweig 1956; Jahrbuch 1956 der Schiffbautechnischen Gesellschaft 50, pp 180-203 (1957).
18. Zysina-Molozhen, L.M. and Kuznetsova, V.M., "Investigation of Turbulent Conditions in a Boundary Layer," Thermal Engineering (Teploenergetika), Vol 16, No 7, pp 16-20 (1969).
19. Schlichting, H., Boundary Layer Theory, Fourth Ed, McGraw-Hill, New York, pp 15-17 (1960).
20. Dryden, H.L., Aerodynamics and Jet Propulsion, Vol V, University Press, Princeton, NJ (1959).
21. Dhawan, S. and Narasimha, R., "Some Properties of Boundary Layer Flow During the Transition from Laminar to Turbulent Motion," Journal of Fluid Mechanics, Vol 3, Pt 4, pp 418-436 (1958).
22. Goldstein, S., Modern Developments in Fluid Dynamics, Vol 2, Oxford Univ Press (1938).
23. Von Karman, T., "Turbulence and Skin Friction," Journal of Aero Sci, Vol 1, No 1, pp 1-20 (1934).
24. Schubauer, G.B. and Klebanoff, P.S., "Contributions on the Mechanics of Boundary Layer Transition," NACA 1289 (1956).
25. Van Driest, E.R. and Boison, J.C., "Experiments on Boundary-Layer Transition at Supersonic Speeds," Journal of Aero Sci, Vol 24, No 12, pp 885-899 (December 1957).
26. Antonia, R.A. and Luxton, R.E., "The Response of a Turbulent Boundary Layer to a Step Change in Surface Roughness. Part 2. Rough-to-Smooth," Journal of Fluid Mechanics, Vol 53, Pt 4, pp 737-757 (1972).

27. Jackson, M.D., Baker, D.L. and Powars, C.A., "PANT Series A Wind Tunnel Test Data Report," Aerotherm Project No 7042, Aerotherm Acurex Corp (December 1972).
28. Anderson, A.D., "Interim Report Passive Nosedip Technology (PANT) Program, Volume 2, Summary of Experimental Results," Appendix A, Aerotherm Report 74-100 (1975).
29. Personal communication between R.L. Baker of The Aerospace Corporation and D.C. Wilcox of DCW Industries (June 1976).
30. Buglia, J.J., "Heat Transfer and Boundary-Layer Transition on a Highly Polished Hemisphere-Cone in Free Flight at Mach Numbers up to 3.14 and Reynolds Numbers up to $24 \cdot 10^6$," NASA TN D-955 (1961).
31. Hall, J.R., Speegle, K.C. and Piland, R.O., "Preliminary Results from a Free-Flight Investigation of Boundary-Layer Transition and Heat Transfer on a Highly Polished 8-Inch-Diameter Hemisphere-Cylinder at Mach Numbers up to 3 and Reynolds Numbers Based on a Length of 1 Foot up to $17.7 \cdot 10^6$," NACA RM L57D18c (1957).
32. Traci, R.M. and Wilcox, D.C., "Freestream Turbulence Effects on Stagnation Point Heat Transfer," AIAA Journal, Vol 13, No 7, pp 890-896 (1975).

BIBLIOGRAPHY

The period of performance on this Contract was January 15, 1974 to July 15, 1976. During that time the following three interim reports describing progress on the Contract were written.

1. Wilcox, D.C., "Turbulence-Model Transition Predictions for Blunt-Body Flows," AFOSR-TR-74-1714 (July 1974).
2. Wilcox, D.C. and Chambers, T.L., "Further Refinement of the Turbulence-Model Transition-Prediction Technique," AFOSR-TR-75-1682 (July 1975).
3. Wilcox, D.C. and Chambers, T.L., "Effects of Surface Heat Transfer on Boundary-Layer Transition," AFOSR-TR-75-1398 (July 1975).

Additionally, three papers have been written which are based on work performed in this Contract. One has appeared in the AIAA Journal while the other two have been presented at AIAA meetings. Another AIAA paper is planned for presentation at the 15th Aerospace Sciences Meeting in Los Angeles, California, in January 1977. The four publications are:

1. Wilcox, D.C., "Turbulence-Model Transition Predictions," AIAA Journal, Vol 13, No 2, pp 241-243 (February 1975).
2. Wilcox, D.C., "Turbulence Model Transition Predictions: Effects of Surface Roughness and Pressure Gradient," AIAA 8th Fluid and Plasma Dynamics Conference, Paper No 75-857, Hartford, Connecticut (June 16-18, 1975).
3. Wilcox, D.C. and Traci, R.M., "A Complete Model of Turbulence," AIAA 9th Fluid and Plasma Dynamics Conference, Paper No 76-351, San Diego, California (July 16-18, 1976).
4. Wilcox, D.C., "A Model for Transitional Flows," Paper to be presented at the AIAA 15th Aerospace Sciences Meeting, Los Angeles, California (January 24-26, 1977).

DISTRIBUTION

Air Force Office of Scientific Research
Bolling AFB, Bldg. 410
Washington, D.C. 20332

Prototype Development Associates, Inc.
1740 Garry Avenue, Suite 201
Santa Ana, California 92705
Attn: J. Dunn

Jet Propulsion Laboratory
Gas Dynamics Section
4800 Oak Grove Drive
Pasadena, California 91109
Attn: J. Kendall
L. Mack

University of Southern California
Dept. of Aerospace Engineering
University Park
Los Angeles, California 90007
Attn: J. Laufer

Lockheed Missiles & Space Co.
Continental Building, Suite 445
101 Continental Boulevard
El Segundo, California 90245
Attn: T. Fortune

AEDC
AFSC, USAF
Arnold Air Force Station
Tennessee 97389
Attn: J. Miller

Flow Research, Inc.
5959 West Century Boulevard, Suite 912
Los Angeles, California 90045
Attn: C. Merkle

Calspan Corporation
P.O. Box 235
Buffalo, New York 14221
Attn: M. Holden

Philco-Ford Corporation
Space & Reentry Systems
Ford Road
Newport Beach, California 92663
Attn: A. Demetriades
C. White

AVCO Corporation
201 Lowell Street
Wilmington, Massachusetts 01887
Attn: A. Pallone
V. DiCristina

General Electric
3198 Chestnut Street
Philadelphia, Pennsylvania 19101
Attn: A. Martellucci

Physical Sciences, Inc.
18 Lakeside Office Park
Wakefield, Massachusetts 01880
Attn: M. Finson

Director of Defense Research and
Engineering (Strategic Weapons)
The Pentagon
Washington, D.C. 20330
Attn: R. Ruffine

Department of Aerospace & Mechanical
Engineering Sciences
University of California
P.O. Box 109
La Jolla, California 92038
Attn: S. Penner

Defense Documentation Center
Cameron Station
Alexandria, Virginia 22314

Applied Physics Laboratories
Johns Hopkins University
Silver Springs, Maryland 20390
Attn: Dr. Stone

Defense Advanced Research Projects
Agency
1400 Wilson Boulevard
Arlington, Virginia 22209
Attn: TIO
K. Kresa
R. Moore

Air University Library
Maxwell Air Force Base
Alabama 36112
Attn: AUL 3T-64-316

Acurex Corporation
485 Clyde Avenue
Mountain View, California 94040
Attn: R. Kendall
R. Rindal

AVCO Everett Research Laboratory
2385 Revere Beach Parkway
Everett, Massachusetts 02149
Attn: K. Wray

DISTRIBUTION (continued)

Boeing Company
Seattle, Washington 98124
Attn: R. Montgomery

Battelle Memorial Institute
505 King Avenue
Columbus, Ohio 43201
Attn: Defender (E. Unger)

Commanding Officer
Ballistics Research Laboratories
Aberdeen Proving Ground, Maryland 21005
Attn: C. Murphy

Arnold Engineering Development Center
Von Karman Gas Dynamics Facility
Tullahoma, Tennessee 37389
Attn: J. Hahn

Office of Naval Research
Department of the Navy
Washington, D.C. 20360
Attn: Phys. Br. (Code 421)
Dr. Isakson

TRW Systems, Inc.
One Space Park
Redondo Beach, California 92078
Attn: L. Hromas

U.S. Army Advanced Ballistic Missile
Defense Agency
Commonwealth Building
1320 Wilson Boulevard
Arlington, Virginia 22209
Attn: CRDABM-RD (Street G)
RP (Rep)
DT (Rep)

Massachusetts Institute of Technology
Lincoln Laboratory
244 Wood Street
Lexington, Massachusetts 02173
Attn: BMRS Project

NASA Scientific & Technical Information
Facility
P.O. Box 33
College Park, Maryland 20740
Attn: Acquisitions BR(S-AK-DL)

California Institute of Technology
Pasadena, California 91109
Attn: L. Lees
H. Liepmann
P. Saffman
D. Knight

AF Cambridge Research Laboratory
Lawrence G. Hanscom Field
Bedford, Massachusetts 01730
Attn: CRMCLR, Stop 29

Air Force Flight Dynamics Laboratory
Wright-Patterson Air Force Base
Ohio 45433
Attn: M. Buck
W. Hankey
J. Shang
K. Stetson

Air Force Materials Laboratory
Wright-Patterson Air Force Base
Ohio 45433
Attn: E. Heinonen

Air Force Weapons Laboratory
Kirtland Air Force Base
Albuquerque, New Mexico 87115
Attn: WLRA/Capt. Koziol
J. Ortwerth
G. Jumper

Commanding General
U.S. Army Safeguard Systems Command
P.O. Box 1500
Huntsville, Alabama 35807
Attn: SENSC-Y

U.S. Naval Surface Weapons Center
White Oak, Silver Springs, MD 20910
Attn: Librarian
D. Reda
C. Lyons
R. Phinney

Institute for Defense Analysis
Science and Technology Division
400 Army-Navy Drive
Arlington, Virginia 22202
Attn: H. Liepmann

Case Western Reserve University
Cleveland, Ohio 44106
Attn: E. Reshotko

NASA Langley Research Center
Hampton, Virginia 23665
Attn: I. Beckwith
J. Harris
D. Bushnell
C. Anderson

DISTRIBUTION (continued)

The RAND Corporation
1700 Main Street
Santa Monica, California 90406
Attn: C. Gazley

NASA Ames Research Center
Moffett Field, California 94035
Attn: M. Rubesin
J. Marvin
B. Baldwin

Space & Missile Systems Organization
P.O. Box 92960
Worldway Postal Center
Los Angeles, California 90009
Attn: T. Hopkins
E. Taylor

The Aerospace Corporation
P.O. Box 92957
Los Angeles, California 90009
Attn: W. Portenier

Naval Underwater Systems Center
Newport, Rhode Island 02840
Attn: G. Christoph

Lawrence Livermore Laboratories
P.O. Box 808
Livermore, California 94550
Attn: A. Buckingham

DCAS
14450 Erwin Street
Van Nuys, California 91408
Attn: H. Moses

U.S. Naval Weapons Laboratory
Dahlgren, Virginia 22448
Attn: Code KRT (MODE)

Los Alamos Scientific Laboratory
Group T-3, Mail Stop 216
P.O. Box 1663
Los Alamos, New Mexico 87544
Attn: J. Ramshaw

University of California, Berkeley
College of Engineering
Berkeley, California 94720
Attn: S. Berger

Stanford University
Dept. of Mechanical Engineering
Palo Alto, California 94305
Attn: W. Reynolds
J. Johnston

END-11-76